Review in Advance first posted online
on September 16, 2008. (Minor changes may
still occur before final publication
online and in print.)

# An Inconvenient Sea Truth: Spread, Steepness, and Skewness of Surface Slopes

## Walter Munk

Scripps Institution of Oceanography, University of California, San Diego, California 92093;
email: wmunk@ucsd.edu

## Key Words

capillary waves, wind stress, shipwaves, microseisms

## Abstract

Bréon and Heriot (BH) have collected eight million globally distributed satellite images of sunglitter, which yield a few simple, robust rules about the statistics of surface slopes: 1) constant angular spread, 2) linear steepness, and 3) sigmoid (near stepwise) skewness (all with respect to wind speed). Yet the information is sparse because it says nothing about time and space scales. The BH rules are an inconvenient sea truth, too fundamental to be ignored, too incomplete to be understood. With regard to BH rule 1 (BH:1), I suggest that the constant spread is associated with a wake-like geometry of the short gravities. Steepness linearity (BH:2) remains an enigma. Skewness (BH:3) appears to be correlated with a rather sudden onset of breaking for winds above 4 m s$^{-1}$. I do not think that skewness comes from parasitic capillaries. These are tentative conclusions; I look forward to intensive sea-going experiments over the next few years demolishing the proposed interpretations.

## 1. INTRODUCTION

The scale of waves contributing to mean square slope is on the order of 1 mm to approximately 1 m, as compared with 1 m to approximately 100 m for the wave energy spectrum. The slope spectrum spans the transition from gravity to capillary waves. Generation of the long energetic gravity waves has long been attributed to the wind shear at the critical layer (Miles 1957); energy transfer is proportional to the amplitude of the waves already present, which leads to quasi-exponential growth. There is no theory for the generation of the short steep gravity waves. Perhaps it is more in line with the resonance theory of Phillips (1957) for pressure spots traveling along the surface, with quasi-linear wave growth independent of the existing waves (as in the case of ship wakes).

Compared with the enormous literature on the long gravity waves, information on the short gravities and capillaries is scarce indeed. Yet from the point of view of the transfer of momentum across the air-sea boundary, the shorter waves are more interesting. Here I discuss the problems, not their solutions. Intensive experiments[1] on the short gravities are scheduled for the next few years.

## 2. THE SLOPE PROBABILITY DISTRIBUTION

**Figures 1** and **2** illustrate the underlying geometry. In a flat calm, a single image of the Sun would appear at the horizontal specular reflection point. But when the water is roughened there are thousands of dancing highlights, each a tiny image of the Sun reflected from an appropriately inclined water facet. The underlying grid gives the required tilt magnitude and azimuth. The variable intensity is then a measure of the probability of slopes. The principle is quite old; Spooner (1822) made four such measurements in the Tyrrhenian Sea.

**Figure 1** illustrates how the setting Sun concentrates the pattern into a narrow street. Of more interest here is the growth of the glitter pattern with wind speed at a fixed (high) solar elevation (**Figure 2**). Because the wavelength of light is short compared with any existing ocean waves the reflections are specular; there is no information on the scale of the reflecting waves. We show below that an important component of the specular scatter is associated with short waves near the transition from gravity to capillary waves (17 mm).

Note that the center of the glitter pattern in the images on the right side of **Figure 2** has shifted downwind from the grid center. This shift can be associated with an up/downwind asymmetry of the wave profile (**Figure 3**). Let

$$\xi = \frac{m_x}{\sigma_x}, \quad \eta = \frac{m_y}{\sigma_y}, \quad \sigma_x^2 = \langle m_x^2 \rangle, \quad \sigma_y^2 = \langle m_y^2 \rangle \tag{1}$$

designate the components of wave slope normalized with respect to root mean square (rms) slope $\sigma$, with $x$ in the downwind direction and $y$ in the crosswind direction [$y$ is upwind for Bréon Henriot (BH) and Cox & Munk (1956) (CM)]. The observations can then be fitted by the following terms in the Gram-Charlier expansion of a nearly gaussian distribution[2]:

$$p(\xi, \eta) = \frac{1}{2\pi} e^{-\frac{1}{2}(\xi^2 + \eta^2)} \left[ 1 + \frac{1}{2} c_{12} \xi(1 - \eta^2) + \frac{1}{6} c_{30} \xi(3 - \xi^2) + \frac{1}{24} c_{40}(3 - 6\xi^2 + \xi^4) \right.$$
$$\left. + \frac{1}{4} c_{22}(1 - \xi^2)(1 - \eta^2) + \frac{1}{24} c_{04}(3 - 6\eta^2 + \eta^4) \right]. \tag{2}$$

We expect (and find) symmetry in the crosswind direction, so that $c_{ij} = 0$ for odd $j$. The seven remaining parameters $\xi^2$, $\eta^2$, $c_{12}$, $c_{30}$, $c_{40}$, $c_{22}$, $c_{04}$ are determined by the observations as

---

[1] Project RaDyO (radiation through a dynamic ocean).

[2] The Cox & Munk (1956) (CM) curve fitting [followed by Bréon-Henriot (BH)] was limited to slopes of less than 2.5 times the root mean square (rms) slopes, and this can lead to significant errors (Wentz 1976). A better procedure is based on the expansion of $\log(p)$ by Chapron et al. (2000).
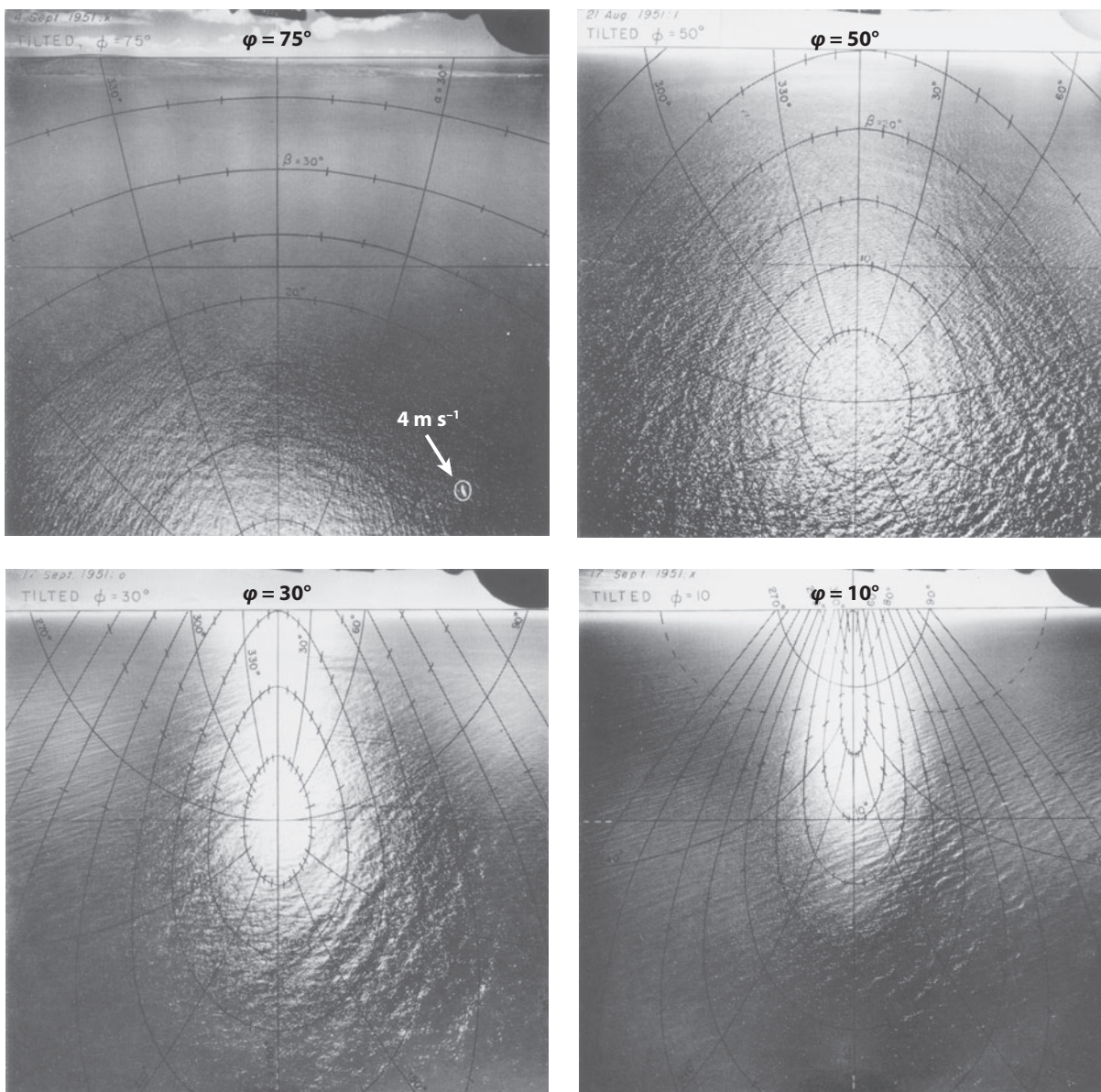
**Figure 1**

The glitter pattern at solar elevations of $\phi = 75°$, $50°$, $30°$, and $10°$. Wind speed is approximately 4 m s$^{-1}$ for all images. The superimposed grids consist of lines of constant slope azimuth $\alpha$ (radial drawn for every 30°), and of constant tilt $\beta$ (closed) for every 5°. The vessel *Reverie* is encircled in the upper left photograph (from Cox & Munk 1956).

functions of wind speed. We require the first five moments:

$$\mu_n = \int_{-\infty}^{\infty} d\eta \int_{-\infty}^{\infty} d\xi \; \xi^n \; p(\xi, \eta),$$

$$\mu_0 = 1, \; \mu_1 = \langle\xi\rangle = 0, \; \mu_2 = \langle\xi^2\rangle = 1, \; \mu_3 = \langle\xi^3\rangle = -c_{30}, \; \mu_4 = \langle\xi^4\rangle = 3 + c_{40}. \quad (3)$$
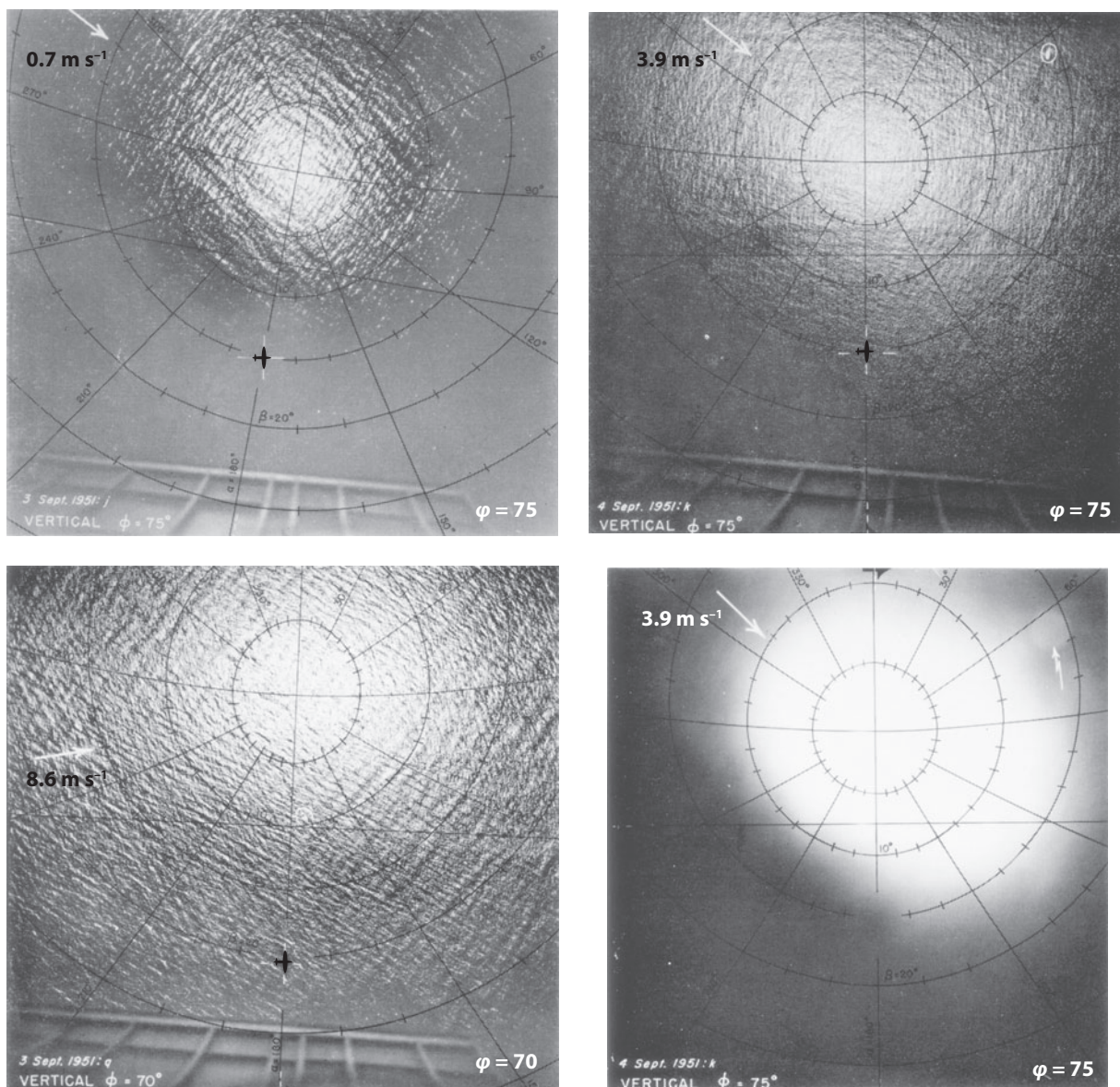
**Figure 2**

The glitter pattern at wind speeds of 0.7, 3.9, and 8.6 m s$^{-1}$ for high solar elevations of $\phi = 75°$, 75°, and 70°. The photometric image of the 3.9 m s$^{-1}$ run (*right bottom*) shows the downwind displacement of the glitter pattern associated with the skewness in the slope distribution. The plane's shadow (*white cross*), barely seen at the antisolar point (180°, 90°-$\phi$), permitted correction for roll, pitch, and yaw of the plane. Large rotation in upper left photograph is due to bad yaw. The position of the vessel *Reverie* is indicated by a white ellipse.
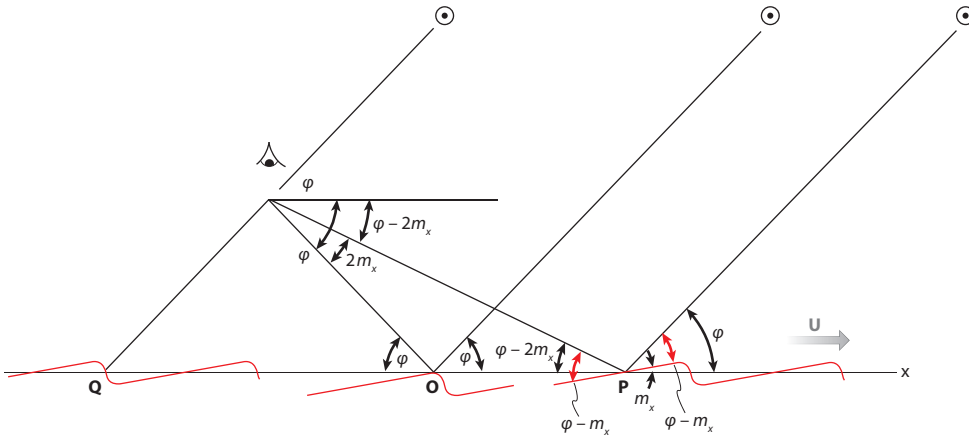
**Figure 3**

The wind is assumed to blow in the x direction toward the Sun (elevation $\phi$). **O** is the specular reflection from a horizontal facet, with incident and reflected inclinations $\phi$. **P** is the specular reflection from a facet windward of the wave crest at inclination $m_x$. For a positive mean slope the mean specular point is shifted in the positive x direction downwind. **Q** is the back reflection from a downwind facet of negative slope (the shadow of the plane is here). In the general case the azimuth of the Sun is $\Psi$ degrees anticlockwise from downwind.

The corresponding raw moments are $\sigma_x^n \mu_n$:

$$1, \quad \langle m_x \rangle = 0, \quad \langle m_x^2 \rangle = \sigma_x^2, \quad \langle m_x^3 \rangle = -c_{30}\,\sigma_x^3, \quad \langle m_x^4 \rangle = (3 + c_{40})\sigma_x^4. \tag{4}$$

The up/downwind skewness and kurtosis (peakedness) are defined as

$$\mu_3 = \langle \xi^3 \rangle = -c_{30}, \quad \mu_4 - 3 = \langle \xi^4 \rangle - 3 = c_{40}.$$

The mean-cubed term is a measure of the up/downwind asymmetry.

The cross-wind symmetry suggests a collapse of the two-dimensional probability distribution onto the $\xi$-axis:

$$p(\xi) = \int_{-\infty}^{\infty} d\eta \; p(\xi, \eta) = \frac{1}{\sqrt{2\pi}} e^{-\frac{1}{2}\xi^2} \left[ 1 + \frac{1}{6} c_{30}\, \xi (3 - \xi^2) + \frac{1}{24} c_{40}(3 - 6\xi^2 + \xi^4) \right]. \tag{5}$$

The dependence on $c_{12}$, $c_{22}$, and $c_{04}$ has disappeared. The moments are the same as in Equation 3.

A slice through the center of the distribution:

$$p_{slice}(\xi) = p(\xi, 0) = \frac{1}{2\pi} e^{-\frac{1}{2}\xi^2} \left[ 1 + \frac{1}{8} c_{04} + \frac{1}{2} c_{12}\xi + \frac{1}{4} c_{22}(1 - \xi^2) \right.$$

$$\left. + \frac{1}{6} c_{30}\, \xi (3 - \xi^2) + \frac{1}{24} c_{40}(3 - 6\xi^2 + \xi^4). \right] \tag{6}$$

has raw moments

$$\frac{1}{\sqrt{2\pi}} \left\{ 1 + \frac{1}{8} c_{04}, \; \frac{1}{2} c_{12}\, \sigma_x, \; \left( 1 + \frac{1}{8} c_{04} - \frac{1}{2} c_{22} \right) \sigma_x^2 \right\}.$$

Note that the zeroth moment is not 1.

The maximum in $p(\xi)$ defines the center of the glitter pattern. Setting $dp/d\xi = 0$ and keeping only the linear terms in $\xi$ yields

$$4c_{30} - (8 + 5\,c_{40})\xi_{max} = 0. \tag{7}$$

The correction for peakedness is small. Setting $c_{40} = 0$ gives

$$\xi_{\max} = \frac{1}{2}c_{30} = -\frac{1}{2}\langle \xi^3 \rangle, \qquad (m_x)_{\max} = -\frac{1}{2}\langle m_x^3 \rangle / \langle m_x^2 \rangle, \tag{8}$$

consistent with Longuet-Higgins (1982). Because $\langle m_x^3 \rangle$ is negative, the center of the glitter pattern is displaced by an angle $2(m_x)_{\max}$ in the positive $x$ direction (**Figure 3**).

## 3. BRÉON-HENROIT (BH) RESULTS

Bréon & Henriot (2006) give the following values for the seven parameters in the Gram-Charlier expansion (Equation 2):

$$\left.\begin{array}{ll} 10^3\,\sigma_x^2 = 1 + 3.16\,U \pm 0.5, & 10^3\,\sigma_y^2 = 3 + 1.85\,U \pm 0.5 \\[4pt] c_{12} = +0.9 \times 10^{-3}\,U^2 \pm 0.01, & c_{30} = +0.45(1 + e^{7-U})^{-1} \pm 0.01 \\[4pt] c_{04} = 0.3 \pm 0.05, \quad c_{22} = 0.12 \pm 0.03, & c_{40} = 0.4 \pm 0.1. \end{array}\right\} \tag{9}$$

Accordingly, the total mean-square slope and the BH ratio (a measure of directivity) are

$$\sigma^2 = \sigma_x^2 + \sigma_y^2 = a + b\,U \pm \varepsilon, \quad a = 4 \times 10^{-3}, \quad b = 5.01 \times 10^{-3}, \quad \varepsilon = 0.71 \times 10^{-3},$$
$$\gamma = \sigma_y^2 / \sigma_x^2 = 0.585 + 0.76\,U^{-1}.$$

We refer to $a$, $b$ as the BH numbers and to $\gamma$ as the BH ratio; $\gamma = 0.66$ for $U = 10$ m s$^{-1}$. Here $U = U_{10}$ in m s$^{-1}$ is derived from satellite scatterometry calibrated by comparison with buoy observations, with an estimated rms error of 1.3 m s$^{-1}$. The standard deviation of wind direction is 17°. 50,000 measurements of wind speed were apportioned into 0.0–0.5, 0.5–1.0, ..., 14.5–15.0 m s$^{-1}$ bins. Almost ten million (!) reflectance measurements distributed globally were available for slope parameter inversions.

In contrast, the 29 CM runs were made within nine days off Maui, Hawaii. The winds were measured on the 58-ft schooner *Reverie* on the fore masthead (41 ft) and bowsprit (10 ft). Masthead winds ranged from 0.7 to 13.8 m s$^{-1}$. Wind direction was estimated by eye.

The estimated CM mean-square slopes $\sigma_x^2$ and $\sigma_y^2$ are in agreement with the BH observations, and well within the BH error bars (**Figure 4a**). However, there is an important deviation of the skewness $c_{30}$ from the CM linear fit, suggesting saturation at high wind speeds. The BH mean peakedness $c_{40}$ is well above the CM estimate.

**Figure 5** shows the raw $p(m_x, m_y)$ and normalized $p(\xi, \eta)$ distributions according to the BH fits (Equation 9). **Figure 6** gives the one-dimensional probability distribution function (pdf). The positive values of $\xi_{\max}$ are related to the fact that more than half the wave length is occupied by a positive slope (upwind from the crest, **Figure 3**). The negative sign of $\langle \xi^3 \rangle$ is related to the steep negative slopes downwind from the crest.

The BH results on skewness and peakedness present a major challenge: how to interpret the saturation skewness

$$\langle \xi^3 \rangle \approx -0.45 \text{ for } U > 10 \text{ m/s}. \tag{10}$$

The results in **Figure 4** and subsequent figures were taken by radiometer POLDER-1 on the platform ADEOS-1. Since then, further measurements with POLDER-2 aboard ADEOS-2 have been analyzed by the same method, leading essentially to the same result (F.M. Bréon, personal communication). Dr. Bréon also kindly furnished me with the numbers used in his plots,[3] permitting the elimination of $U_{10}$ as an independent variable (**Figure 7**). I prefer this plot of mean-cube

---

[3]We have replaced the Bréon-Henriot (BH) value for $\langle m^2 \rangle$ in the weakest wind bin ($0 < U < 0.5$ ms) by $\langle m_x^2 \rangle = 0$.
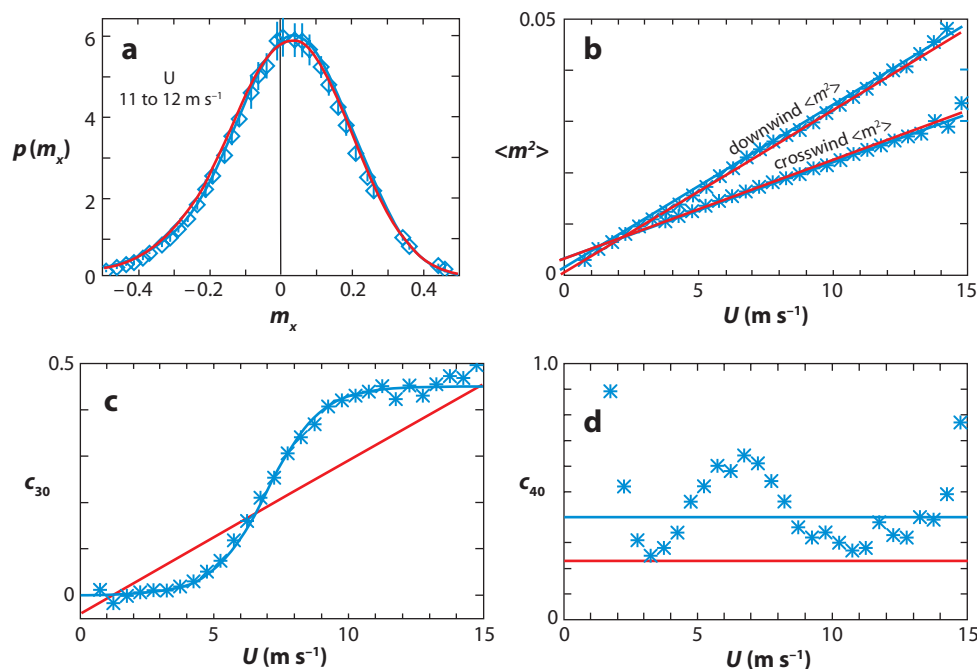
**Figure 4**

Comparison of Bréon & Henriot 2006 (BH) (*blue, with error bars*) to Cox & Munk 1956 (CM) (*red*). (*a*) The probability function $p(m_x)$ is a projection onto the x-axis of a two dimensional distribution. (*b*) BH and CM components in slope variance are in good agreement. (*c*) The skewness parameter $c_{30}$ saturates at $U = 10$ m s$^{-1}$, unlike the linear CM relation. (*d*) Peakedness $c_{40}$.

slope against mean-square slope in as much as the wind speed is relatively poorly determined, and there is some danger of circular reasoning extending the linear BH dependence of $\langle m^2 \rangle$ on $U$ to the weak wind data (see **footnote 2**). Further, in any comparison of laboratory and field measurements it is better to use field and laboratory wave slopes as a reference for comparison, and not assume any relations between masthead and laboratory winds.

It is convenient to fit the data to a formula. BH use the representations

$$\langle m^2 \rangle = (4 + 5.01\, U)\, 10^{-3}, \qquad \langle m^3 \rangle_{norm} = -0.45(1 + e^{7-U})$$

and the red curve in **Figure 7** is obtained by eliminating $U$ between the two equations. The sigmoid shape suggests the use of the incomplete Beta function[4] (**Figure 7**)

$$B_z(a,\ b) = \int_0^z t^{a-1}\, (1-t)^{b-1} dt \tag{11}$$

with the asymptotic relations

$$\begin{aligned} B_z(a,\ b) &= a^{-1} z^a \quad &&\text{for} \quad z \ll 1, \\ &= b^{-1}(1-z)^b \quad &&\text{for} \quad 1-z \ll 1. \end{aligned} \tag{12}$$

---

[4]The Beta constants (*a, b*) are different from the Bréon Henriot (BH) constants (*a, b*).
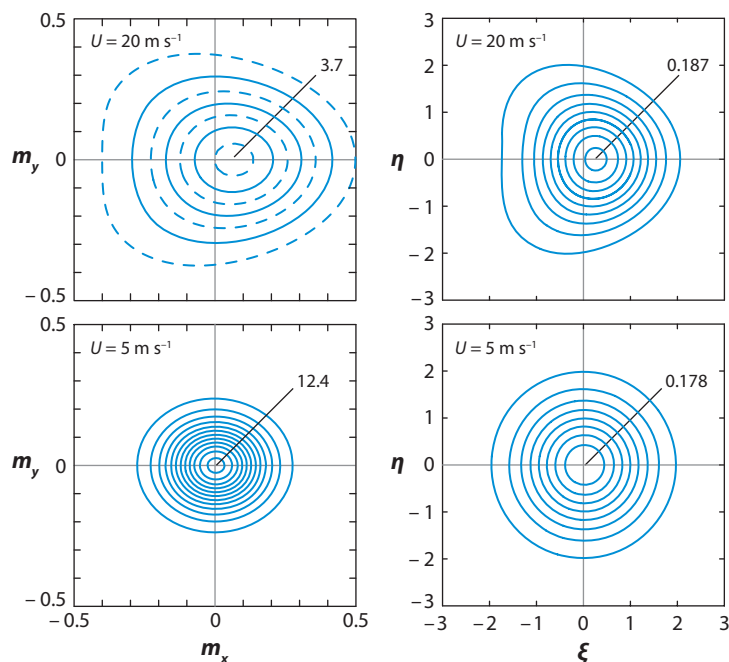
**Figure 5**

Probability density functions of the slope $m_x$, $m_y$ (*left*) and of normalized slope $\xi = m_x/\sigma_x$, $\eta = m_y/\sigma_y$ (*right*) at winds $U = 5$ m s$^{-1}$ (*bottom*) and 20 m s$^{-1}$ (*top*). Volumes beneath the probability distribution function (pdf) surfaces are unity. Mean slope components are zero. The pattern of raw pdfs (*left*) grows with increasing wind speed. Contours for the un-normalized pdfs are elliptical because up-down wind slope variances are larger than cross-wind variances, and they are asymmetrical with the most probable slope displaced in the positive x-direction (downwind).
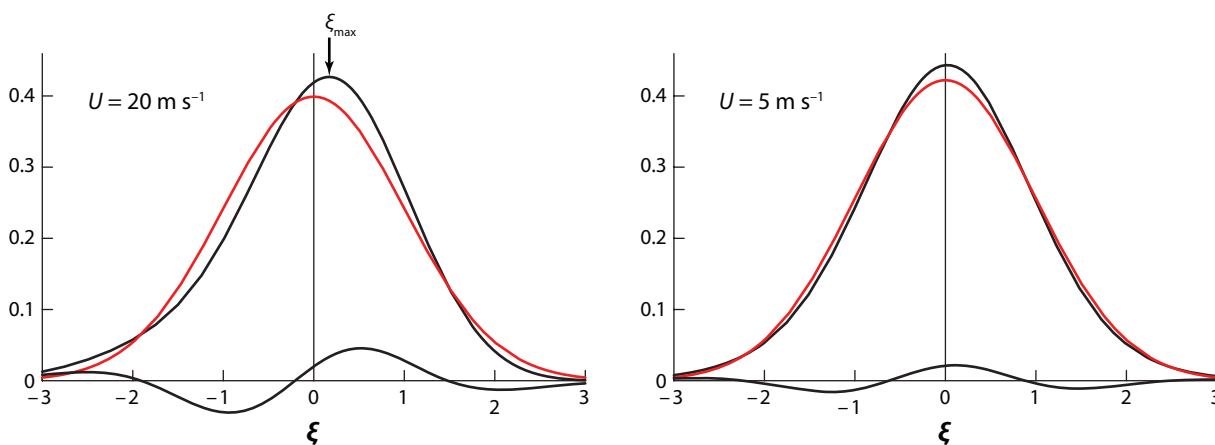


**Figure 6**

One-dimensional probability distribution function (pdf) relative to the gaussian pdf (*red*) for $U = 5$ m s$^{-1}$ and 20 m s$^{-1}$. The most probable slope is positive (upward in the downwind direction), with mode $\xi_{max} = +0.021$, $+0.170$ for $U = 5$, 20 m s$^{-1}$. Surfaces of small positive slope are more probable than those of negative slope; large positive slopes are less probable than large negative slopes, thus permitting the restraint of a zero mean slope.

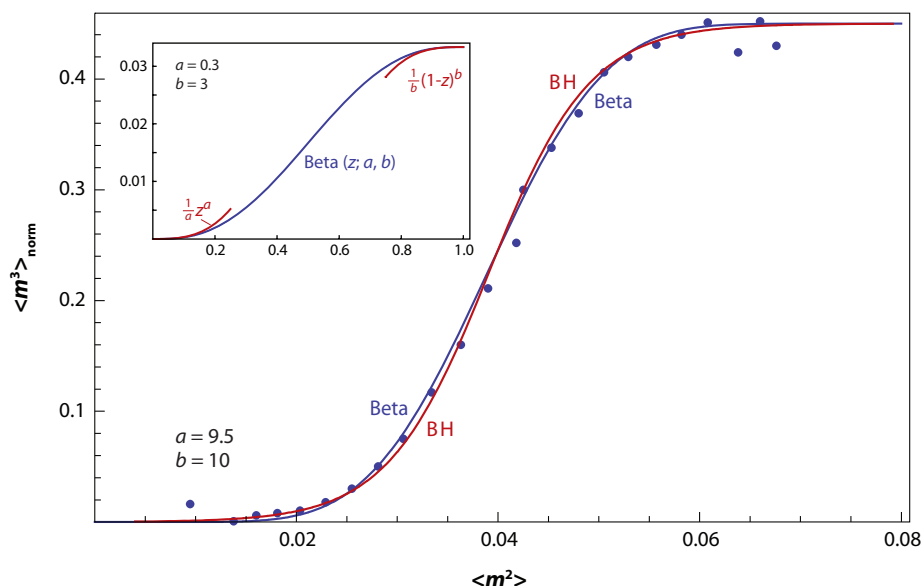**Figure 7**

Bréon Henriot (BH) relation of normalized mean-cube slope as function of the mean-square slope
$\langle m^2 \rangle = \langle m_x^2 \rangle + \langle m_y^2 \rangle$. Red curve is BH fit to an exponential function, blue curve is fit to Beta function. Inset:
the function Beta $(z;\ a,\ b)$ has the required sigmoid signature. For low winds (small $z$) and for saturation
($z$ near 1), Beta can be represented by simple asymptotes.

As shown below, this expression relates the coefficient $a$ to the low wind conditions, and relates
$b$ to the saturation condition (presumably due to breaking). The transition at the inflection point
occurs at

$$z_{\text{infl}} = \frac{a-1}{a+b-2}.$$

For
$$a \ll 1, \quad z_{\text{infl}} \approx 1, \quad \langle m^2 \rangle \approx 0.08, \quad \langle m^3 \rangle \approx -0.45$$
$$b \ll 1, \quad z_{\text{infl}} \approx 0, \quad \langle m^2 \rangle \approx 0, \quad \langle m^3 \rangle \approx 0$$
$$a = b, \quad z_{\text{infl}} = \frac{1}{2}, \quad \langle m^2 \rangle \approx 0.04, \quad \langle m^3 \rangle \approx -0.225.$$

The last case is close to the BH situation. The mean-cube transition from low values to saturation
is remarkably sharp and requires large $a$, $b$ coefficients.

For a fit to the BH relation in **Figure 7**,

$$\langle m^3 \rangle_{norm} = \langle m^3 \rangle_{\max} \phi(\langle m^2 \rangle), \quad \phi(\langle m^2 \rangle) = B_z(a,\ b)/B_1(a,\ b),$$
$$\langle m^3 \rangle_{\max} = -.45, \quad z = \langle m^2 \rangle / \langle m^2 \rangle_{\max}, \quad \langle m^2 \rangle_{\max} = 0.08, \quad a = 9.5, \quad b = 10. \quad (13)$$

The BH and Beta functions both give satisfactory fit to the data (**Figure 7**), which is not surprising
because $\phi$ has four tunable coefficients.

## 4. OIL ON WATER

The BH probability distributions give no information on the lengths of the waves that contribute
to the measured slope statistics. However, there is some qualitative evidence from two experiments
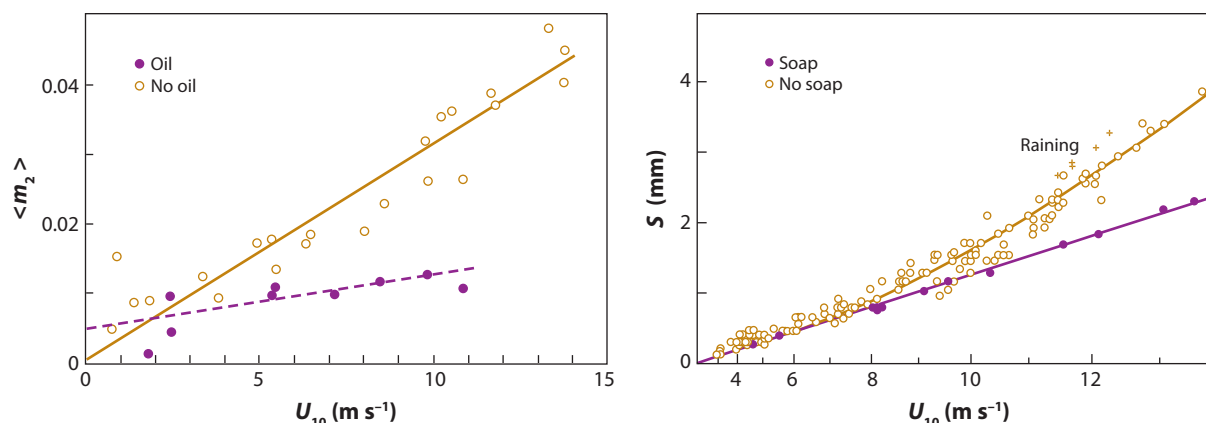
**Figure 8**

(*a*) Up-down wind component of mean-square slopes ⟨$m_2$⟩ for a clean sea surface (*tan*, *open circles*) and a surface covered by an oil slick (*purple*, *solid circles*), from Cox & Munk (1956). (*b*) Wind-induced setup of the surface of a 220-m long 1.85-m deep model-yacht basin as function of the square of windspeed, with and without detergent (Van Dorn 1953).

(**Figure 8**) concerning the effect of oil and soap on the mean-square slope (Cox & Munk 1956) and on wind stress (Van Dorn 1953). For a 10 m s$^{-1}$ wind, the up-down wind component of mean-square slope was reduced by 60% and drag was reduced by 40%. Rapid attenuation of waves is associated with short waves, 10 cm or less, say, and I infer that most of the mean-square slope and a significant fraction of the stress can be attributed to these scales.

The experimental procedures for slope and stress were quite different. For the glitter experiment, oil was pumped on the water by the *Reverie* (**Figure 9**). An optimum mixture consisted of 40% used crank case oil, 40% diesel oil, and 20% fish oil. At moderate winds, 200 gallons of this mixture could be laid in 25 minutes to form a coherent slick of 2000 × 2000 feet. For the wind stress experiment it required the combined effort of three people running at top speed to spread Merrill's Rich Suds at the rate of 60 pounds per hour from the upwind end of the model basin. The two 50-year-old experiments provide vivid evidence that slope and drag are associated with the high-frequency tail of the wave spectrum (as is well known); the present environmental climate does not favor an active continuation of this type of experimentation.

It is difficult to compare the results of the two experiments in any detail. Van Dorn (1953) measured the downwind setup (1.75 ± 0.10 mm at 10 m s$^{-1}$ winds), and inferred a surface stress of 0.1 N/m$^2$ per mm of setup (this allows for the drag along the shallow bottom). Van Dorn noted a "glassy-calm" appearance for $U_{10} < 2$ m s$^{-1}$, and "incipient rippling in patches" for winds up to 4 m s$^{-1}$. The surface "became covered with persistent wavelets" at $U_{10}$ above 4 m s$^{-1}$. Surface currents (on the order of 1% of the wind speed) were unaffected by the detergent.

Van Dorn (referring to previous work by Keulegan 1951) attributes the setup to the sum of two terms,

$$S = AU^2, \qquad S = AU^2 + B(U - U_c)^2 \qquad (14)$$

for $U < U_c$ and $U > U_c$, respectively, with the transition indefinitely postponed when soap is added; $U_c$ is estimated at 5.6 m s$^{-1}$. Van Dorn attributes $S = AU^2$ to a "frictional drag" and the additional term $B(U - U_c)^2$ to wave drag. As an aside, an additional setup associated with a rainstorm could be reconciled with the expected momentum transport of the rain drops.

Cox & Munk (1956) note that the effect of the slick is to "reduce the mean-square slopes by factor of two or three," and "to eliminate skewness." They attribute the effect to the suppression

**Figure 9**

Two successive photographs of glitter within a 2000 × 2000 ft coherent slick band extending from AA to BB. The oil was pumped on the water by the *Reverie* and comprised 40% used crankcase oil, 40% diesel, and 20% fish oil. Wind direction (*white arrow*) and plane shadow (*white cross*) are indicated. Note the downwind displacement of the glitter pattern in the oil-free area.

of waves with periods less than 0.5 seconds ($\lambda = 0.4$ m, $C = 0.8$ m s$^{-1}$), with an $e^{-1}$ decay distance of 1.5 km associated with molecular viscosity. For orientation, waves of minimum phase velocity of 0.23 m s$^{-1}$ are associated with a period of 0.074 s, a length of 17 mm, and an $e^{-1}$ decay of 0.8 m.

A large portion of stress and skewness is associated with (*a*) capillaries and (*b*) short gravities [adjacent to the gravity-capillary (gc) transition], but not all! It has been observed that the drag

coefficient is higher over a young sea than over a mature sea at comparable winds, indicating some role of the longer gravity waves.

## 5. STEEPNESS

Here we attempt to interpret the BH measurements of slope variance:

$$\langle m^2 \rangle = \langle m_x^2 \rangle + \langle m_y^2 \rangle = a + bU, \quad a = 4 \times 10^{-3}, \quad b \approx 5.01 \times 10^{-3} \text{ s/m}.$$

The linearity in the wind dependence imposes severe restrictions on any model for the slope spectra. Starting in 1950, there is a vast literature on elevation (energy) spectra, dominated by the work of Owen Phillips. It is straightforward to infer the slope spectrum from the elevation spectrum; extrapolating to high frequencies then yields mean-square slopes of magnitude comparable to the BH values but with a logarithmic wind dependence incompatible with the BH linear dependence. I have not been able to resolve this incompatibility.

### 5.1. Inference from Elevation Spectra

Write

$$\langle m^2 \rangle = \int_0^\infty \kappa^2 F_\zeta(\kappa) \kappa \, d\kappa,$$

where $F_\zeta(\kappa)$ is the elevation (energy) spectrum.[5] The slope spectrum $\kappa^2 F_\zeta(\kappa)$ is dominated by waves of small scales with short time constants that can adjust to the variable wind field. Here we assume that the slope spectrum is in equilibrium with the local wind. The simplicity and consistency of the BH statistics collected globally without regard to the weather situations would support this assumption.

**5.1.1. Neumann spectrum.** When Cox & Munk (1956) proposed the linear dependence of slope variance on wind, the ultrared $\omega^{-6}$ energy spectrum of Neumann (1953) was fashionable:

$$F_\zeta(\omega) = \pi^3 N g^2 \omega^{-6}, \quad F_\zeta(\kappa) = \frac{1}{2}\pi^3 N g^{-\frac{1}{2}} \kappa^{-4\frac{1}{2}}, \tag{15}$$

where $N = 0.83 \times 10^{-3} \text{s}^{-1}$. Hence $F_m(\kappa) = \kappa^2 F_\zeta(\kappa)$ and

$$\langle m^2 \rangle = \int_{\kappa_0}^\infty \kappa F_m(\kappa) d\kappa = \pi^3 N g^{-\frac{1}{2}} \kappa_0^{-\frac{1}{2}} = \pi^3 N g^{-1} U = 2.6 \times 10^{-3} U$$

for $\kappa_0 = g/C^2 = g/U^2$. This result is in rough agreement with the BH relation $\langle m^2 \rangle = 5 \times 10^{-3} U$. At the time, this result was considered to be an affirmation of the Neumann spectrum.

**5.1.2. Phillips spectra.** Subsequent measurements decisively favored the $\omega^{-5}$ Phillips (1958) spectrum:

$$F_\zeta(\omega) = \beta g^2 \omega^{-5}, \quad F_\zeta(\kappa) = \frac{1}{2}\beta \kappa^{-4}, \quad \beta = 1.2 \times 10^{-2}.$$

Then, with $F_m(\kappa) = \kappa^2 F_\zeta(\kappa) = \frac{1}{2}\beta \kappa^{-2}$,

$$\langle m^2 \rangle = \int_{\kappa_0}^{\kappa_{upper}} \kappa F_m(\kappa) d\kappa = \frac{1}{2}\beta \ln \frac{\kappa_{upper}}{\kappa_0} = \beta \ln \frac{U}{\sqrt{g/\kappa_{upper}}}.$$

The logarithmic dependence on wind speed is in stark contrast to the linear BH dependence.

---

[5] See Appendix B for spectral notation.

In a further move toward deredning the gravity wave spectrum, Phillips (1985) introduced the $\omega^{-4}$ spectrum,

$$F_\zeta(\omega) = \alpha U_* g \omega^{-4}, \quad F_\zeta(\kappa) = \frac{1}{2}\alpha U_* g^{-\frac{1}{2}}\kappa^{-3\frac{1}{2}}. \tag{16}$$

**5.1.3. Banner spectrum.** Banner et al. (1989) made a stereophotogrammetric determination of the wavenumber spectrum from an oil platform under open-sea conditions. Wavenumbers range from 0.5 to 5 cycles per meter (cpm) (the upper limit is far short of the gc transition at 59 cpm). Banner (1990) obtained an optimal fit by a composite spectrum, with a Phillips (1985) $\kappa^{-3\frac{1}{2}}$ dependence near the wind cut-off $\kappa_0$ transiting to the older, Phillips (1958) $\kappa^{-4}$ dependence at $\kappa_1$ (**Figure 10**). We refer to these as the BP85 and BP58 spectra. Banner et al. (1989) write

$$G_\zeta(k) = Ak^{-3}\mathrm{m}^2/\mathrm{cpm}, \quad A = 10^{-4}, \quad \kappa_1 \le \kappa \le \kappa_2 \tag{17}$$

for the one-dimensional BP58 spectrum in cyclical units, corresponding to $\beta = 8\pi^2 A = 0.8 \times 10^{-2}$ [Phillips (1958) has $\beta = 1.2 \times 10^{-2}$]. The inferred slope spectrum is then

$$G_m(k) = 4\pi^2 Ak^{-1}\mathrm{slope}^2/\mathrm{cpm}. \tag{18}$$

Ignoring the BP85 segment for the moment,

$$\langle m^2 \rangle = \int_{k_0}^{k_2} G_m(k)\,dk = 4\pi^2 A\ln(k_2/k_0) = 8\pi^2 A\ln\frac{U}{\sqrt{g/(2\pi k_2)}}, \tag{19}$$

where $k_0 = g/(2\pi U^2)$. For a wind speed $U = 10$ m s$^{-1}$, and the experimental resolution $k_2 = 5$ cpm, $\langle m^2 \rangle = 0.027$ compared with the BH value of 0.05.

The case $k_2 = 5$ cpm is in remarkable agreement with the Cox & Munk (1956) measurements for an oil-covered sea (see **Supplemental Figure 1**; follow the **Supplemental Material link** from the Annual Reviews home page at **http://www.annualreviews.org**), as pointed out long ago by Cox (1958). It is tempting to conclude that the capillaries have been eliminated by the oil slick, leaving the gravity waves whose mean-square slope is in accord with the Banner spectrum. It would follow that the wedge-like area between the white and black points is ascribed to the capillaries generated by some independent process.

## 5.2. Extension to High Frequencies

Following the Phillips (1985) paper, Donelan et al. (1985), Jähne & Riemer (1990), Banner et al. (1989), Banner (1990), and Elfouhaily et al. (1997) reviewed the subject and extended the spectral models to the higher wavenumbers. Most of the discussion refers to the one-dimensional "saturation spectrum" (introduced by Phillips):

$$G_s(\kappa) \equiv \kappa G_m(\kappa) = \kappa^3 G_\zeta(\kappa) = \kappa^4 F_\zeta(\kappa). \tag{20}$$

The Banner saturation spectrum is

$$G_s(\kappa) = \kappa G_m(\kappa) = kG_m(k) = 4\pi^2 A = 4 \times 10^{-3}(\text{dimensionless}). \tag{21}$$

**Figure 11** summarizes the saturation spectrum at the gc transition. The Elfouhaily et al. (1997) measurements give an enhanced wind-dependent intensity centered at the transition. Some recent measurements by Hwang (2005) place the peak to the left of the transition (short gravities) with a gap at the transition; with increasing wind speed the peak shifts toward the transition (the opposite holds for the Cox-Zhang laboratory experiments). **Figure 11***b* is a crude attempt to summarize the situation (see below).
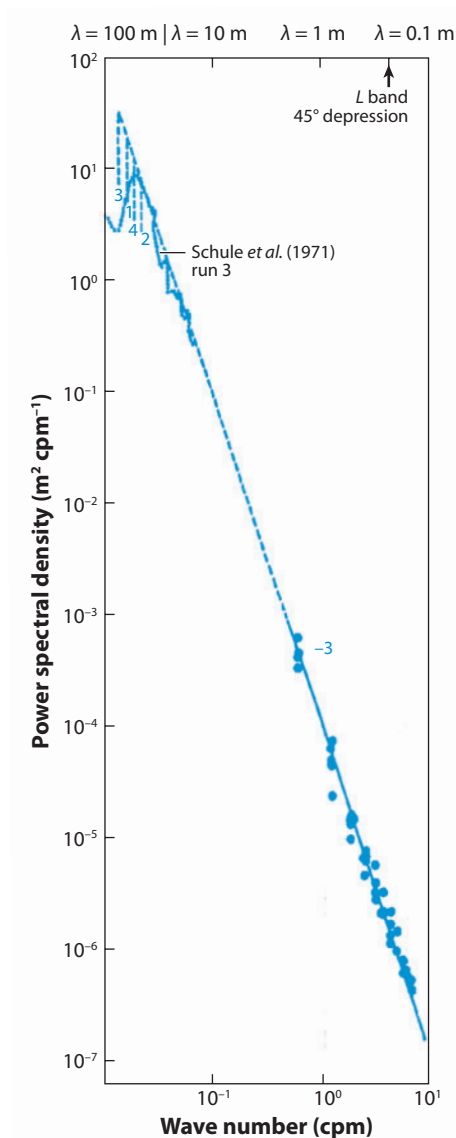
**Figure 10**

The spectrum $\int_{-\infty}^{\infty} F_{\xi}(k_x, k_y)dk_y = 10^{-4} k^{-3}$ m$^2$ cpm$^{-1}$ according to Banner et al. (1989). There is an indication of reduced slope (such as $k^{-5/2}$) at the low wavenumbers.

## 5.3. Cox-Zhang Laboratory Experiments

The scale of the gc transition is well adapted to laboratory experiments. In the Cox & Zhang (C. Cox & X. Zhang, manuscript in preparation) experiments, a narrow laser beam from above is refracted at the wavy surface and recorded beneath the surface, thus yielding $m_x(t)$ and $m_y(t)$. Veron & Melville (2001) use a color imaging slope gauge to derive $m_x(x, y)$ and $m_y(x, y)$. Results are comparable (**Figure 12**). The measurements are easier in the time domain, and more readily interpretable in the space domain. Some results of the Cox & Zhang experiments are summarized in **Table 1**.
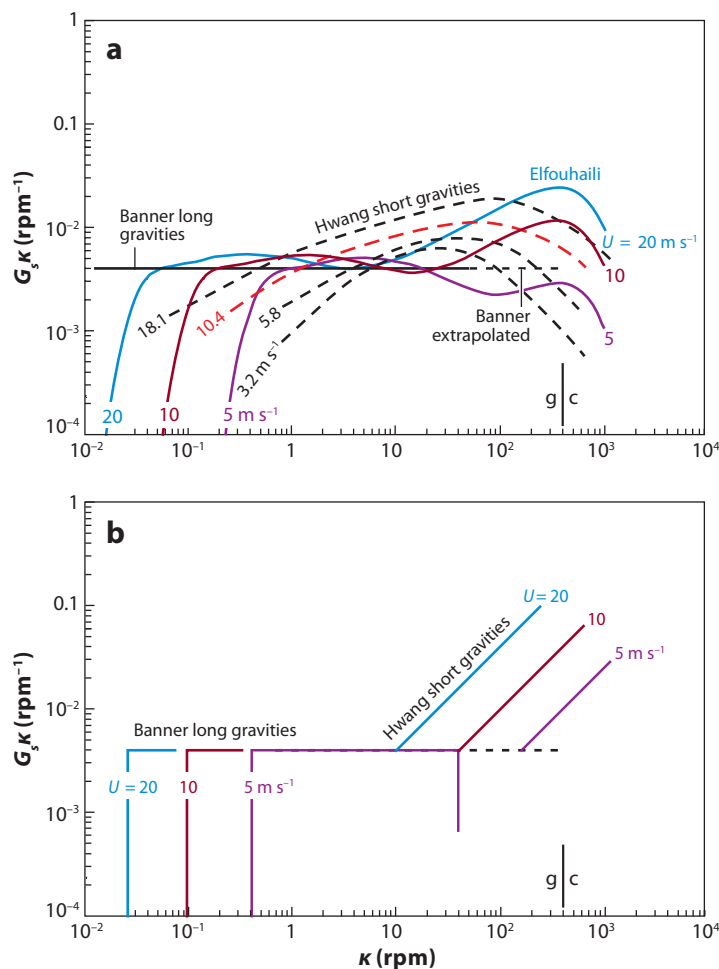
**Figure 11**

The saturation spectrum $G_s(\kappa)$. (*a*) The Banner BP58 spectrum (ignoring BP85) for long gravity waves is extended to the Banner limit of 31 rpm. The Elfouhaily et al. (1997) spectra (*solid curves*) are peaked at the gravity-capillary (gc) transition. Hwang (2005) spectra (*dashed*) are peaked in the short gravity wave band. (*b*) Idealized representation of the saturation spectrum. The transition from the Banner-like white spectrum with low-frequency wind cut-offs to the Hwang spectra is not clear.

These experiments produced a number of significant results. (*a*) The measurements show a gap at the gc transition that separates a moderately narrow peak on the gravity side from a flat, broad plateau at the capillary side. (*b*) For the wind-generated waves the contributions to the mean-square slope from the capillary side are comparable to those from the gravity side and need to be taken into account in any reasonable discussion of the wave statistics; paddle-generated waves have a much smaller capillary component. (*c*) Comparisons with field measurements are difficult because of the interpretation of wind speed and other factors. We note that for $U \approx 5$ m s$^{-1}$ the Hwang slope spectrum peaks at 5 cpm (**Figure 11**) and the Cox & Zhang (CZ) spectrum peaks at 4 Hz or 10 cpm (**Figures 12** and **13**). (*d*) The relative contribution to the mean-square slope from cross-wind slope is less than for the BH open sea measurements, as might be expected from wind generation in a narrow tank (see Section 6).
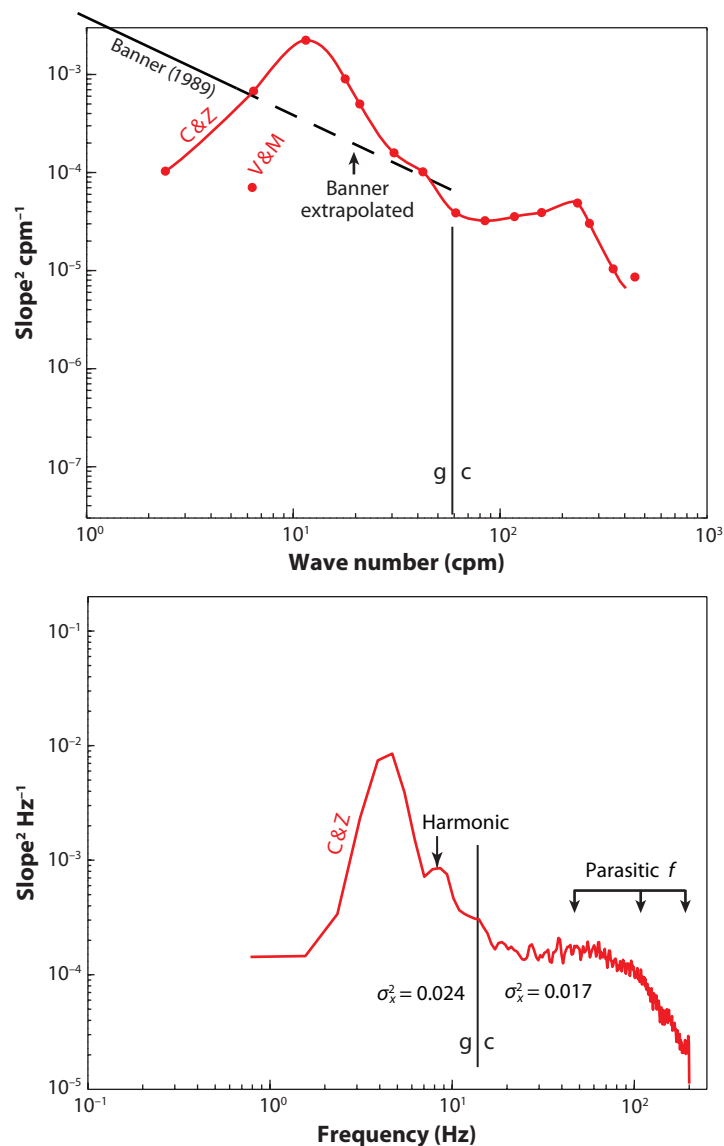
**Figure 12**

Laboratory spectra $F_m(k)$ of Veron & Melville (2001) in wave number space (*upper panel, dashed*) and $F_m(f)$ of C. Cox & X. Zhang (manuscript in preparation) in frequency space (*lower panel, solid*). The Cox & Zhang spectra were transferred into wave number space (*upper panel, solid*). The laboratory spectra show a strong peak on the gravity side of the gravity-capillary (gc) transition and a broad spectral plateau associated with the parasitic capillaries.

## 5.4. Evidence from Microseisms

Some unexpected evidence comes from measurements of pressure fluctuations on the deep sea floor (W. Farrell & W.H. Munk, manuscript submitted). Microseismic noise at frequencies on the order of 0.2 Hz has long been attributed to the effect of oppositely traveling surface waves (surface wave length λ on the order of 100 m). Pressure fluctuations are excited at twice the surface wave

**Table 1    Ratios of mean squares from Cox & Zhang[1]**

| 1. Directivity $\langle 1000\, m_y^2 \rangle / 1000 \langle m_x^2 \rangle$ | | | |
|---|---|---|---|
| | gravity $g$ | capillary $c$ | Total $g + c$ | BH[2] |
| wind | $5.6/20 = 0.28$ | $5.2/18.5 = 0.28$ | $11/39 = 0.28$ | 0.7 |
| paddle | $6.3/35 = 0.018$ | $0.2/3.5 = 0.080$ | $0.086/39 = 0.023$ | |
| 2. Color $\langle 1000\, m_c^2 / 1000\, m_g^2 \rangle$ | | | |
| | downwind $x$ | crosswind $y$ | total $x + y$ | |
| wind | $18.5/20 = 0.93$ | $5.2/5.6 = 0.93$ | $24/25.6 = 0.93$ | |
| paddle | $3.5/35 = 0.10$ | $0.2/.63 = 0.32$ | $3.52/35.6 = 0.10$ | |

[1] Manuscript in preparation.
[2] Bréon & Henriot (2006).

frequency by the Longuet-Higgins (1950) wave-wave interaction mechanism. Webb & Cox (1986) extended the frequency range to approximately 2 Hz ($\lambda = 40$ cm). Here we suggest that pressure measurements up to 27 Hz give information about the transition from long to short gravity waves.

The curves in **Figure 14** are the computed pressure spectrum $F_p(\omega_p)$ in response to surface wave spectra $F_\xi(\kappa)$ according to Hughes (1976):

$$F_p(\omega_p) = \frac{1}{8}\pi \left( \frac{\rho}{C} \right)^2 \omega_p^6 \frac{\kappa F_\xi^2(\kappa)}{\partial \omega_\zeta / \partial \kappa} I, \quad \omega_p = 2\omega_\zeta, \tag{22}$$

where $C = 1500$ m s$^{-1}$ is the mean speed of sound and $I$ is the directional overlap integral (introduced in Section 6; for details see W. Farrell & W.H. Munk, manuscript submitted). Dots
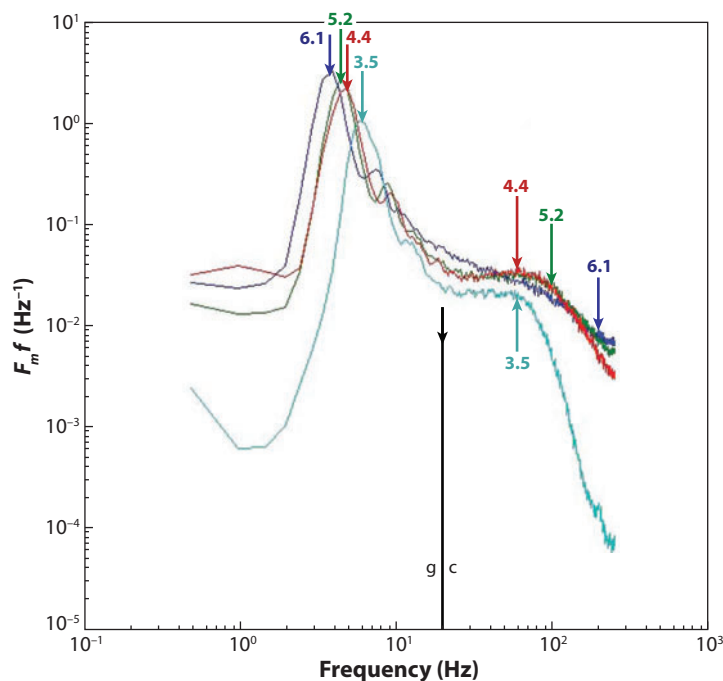


**Figure 13**

Cox-Zhang laboratory slope spectra at stated wind speeds (m s$^{-1}$). Arrows on the capillary side are drawn for parasitic resonance, $C_g = C_c$.
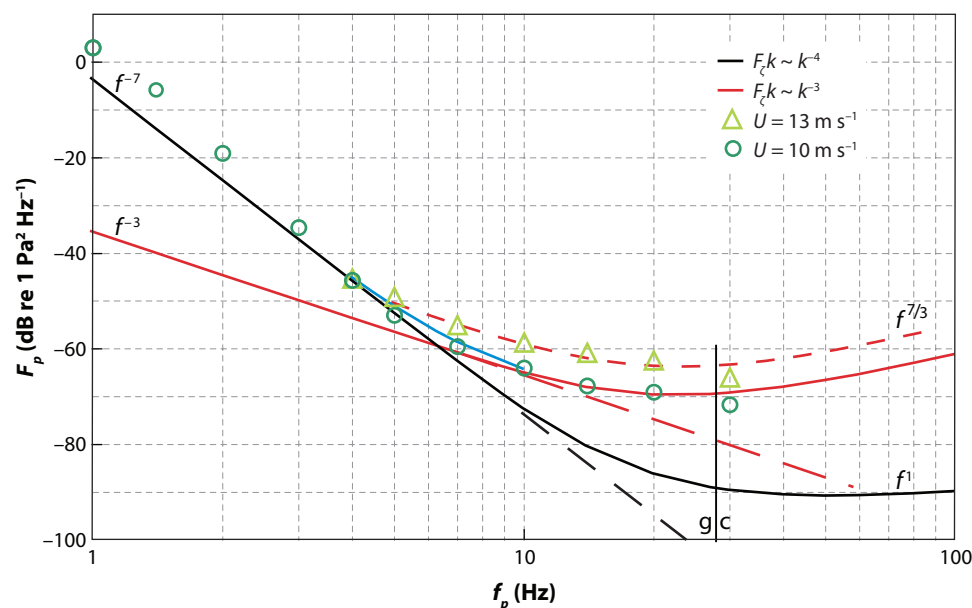
**Figure 14**

Power spectra of deep ocean pressure fluctuation. Dots show the measured Holu spectrum (McCreery et al. 1993) for 10 m s$^{-1}$ winds (*circles*) and 13 m s$^{-1}$ winds (*triangles*). The black curve is the computed pressure spectrum for the Phillips (1958) $\kappa^{-4}$ long surface wave spectrum (the dashed extension is for a gravity-only ocean). Red curves are computed pressure spectra for $\kappa^{-3}$ short surface wave spectra. Computed spectra assume the value of the spreading integral is 0.2.

denote measurements from the Wake Island Array (McCreery et al. 1993) in 5500 m. The black curve is the special case in response to a $f^{-5}$ or $\kappa^{-4}$BP58 surface wave spectrum. Consider that the Phillips spectrum extends indefinitely to higher frequencies. The black curve would then continue indefinitely along a $f^{-7}$ slope provided surface tension was neglected (black dashed line). When surface tension is taken into account, the computed pressure spectrum curves up-wards from the linear extension for $f < 10$ Hz. Starting from the left, the measured pressure spectrum (green points) follows a straight black $f^{-7}$ line, which is the appropriate slope for the $f^{-5}$BP58 surface wave spectrum in a gravity-only ocean. In fact, the transition is at 6 Hz (3 Hz or 5.6 cpm surface wave frequencies) and is in response not to surface tension, but to a transition of the surface waves spectrum from a BP58 $f^{-5}$ dependence to something like a $f^{-3}$ dependence. This important transition from long to short gravity waves is roughly consistent with the Hwang surface measurements.

The red curve in **Figure 14** designates the bottom pressure spectrum for the proposed $f^{-3}$ or $\kappa^{-3}$ surface wave spectrum of short gravities, with the dashed extension corresponding again to a gravity-only ocean. We notice also that the measured pressures at different wind speeds coalesce at the black curve, whereas distinct red curves, separated by 6 dB, need to be drawn for the two wind speeds. Accordingly, the transition marks the change from a saturated long gravity wave spectrum to an unsaturated short gravity wave spectrum. Further, the very existence of the deep pressure fluctuations is evidence for oppositely traveling surface waves and imposes integral restraints on the directional spread (see below). We may expect further critical information from improved future deep pressure measurements.
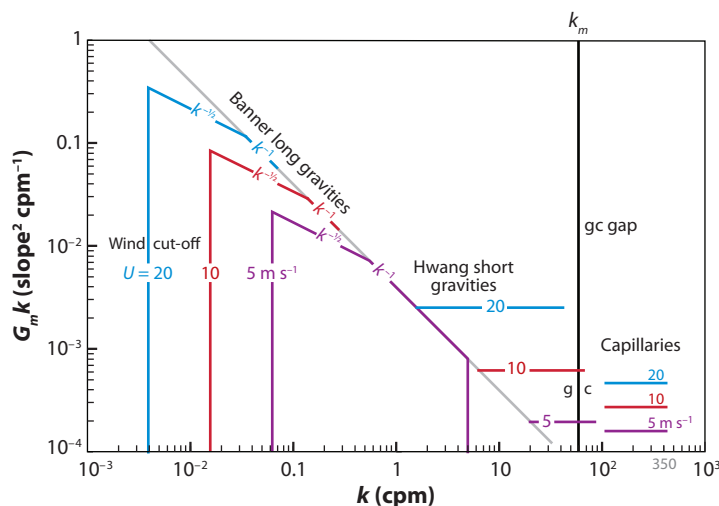
**Figure 15**

The assumed slope spectrum consists of (*i*) the long gravity Banner $k^{-1/2}$ spectrum (BP85) with low-frequency wind-dependent cutoffs, (*ii*) the long gravity Banner $k^{-1}$ spectrum (BP58) with upper cutoffs at 5 cpm, (*iii*) a level spectrum for short gravities (ignoring spectral gap), and (*iv*) capillaries assumed (unrealistically) to make equal contributions to mean square slope; (*iii*) and (*iv*) are separated by a two octave gap (vertical gray band) centered on the gravity-capillary (gc) transisiton.

## 5.5. A Model Slope Spectrum

The model slope spectra consist of four separate features (**Figure 15**): (*a*) a BP85 $\kappa^{-\frac{1}{2}}$ spectrum between the wind cut-off $\kappa_0 = g/U^2$ and a transition wavenumber $\kappa_1$, (*b*) a BP58 $= \frac{1}{2}\beta\kappa^{-1}$ spectrum between $\kappa_1$ and $\kappa_2$, (*c*) a spectrum of short gravities, and (*d*) capillaries separated by a gap at the gc transition.

**5.5.1. Gravity waves.** **Table 2** summarizes the situation. Continuity at the transition wavenumbers uniquely defines the spectral densities (line 7) and their contributions to the mean square slope (line 8). For $\beta = 0.008$,

$$\langle m^2 \rangle_{grav} = 0.004 + 0.016 + 0.021 = 0.041$$

for the contributions of the gravities (very long, long, and short) at $U = 10$ m s$^{-1}$, compared with the BH value of $bU = 0.005 \times 10 = 0.051$, including capillaries.

Suppose the short gravity mean-square slope grows linearly with wind, $\langle m^2 \rangle_{sg} = 0.0205,\ 0.041,\ 0.082$ for $U = 5, 10, 20$ m s$^{-1}$. The corresponding band widths for the short gravities are

$$\kappa_3 - \kappa_2 = 2\beta^{-1}\kappa_2 \langle m^2 \rangle_{sg} = 105,\ 210,\ 420 \text{ rpm}$$

or $\kappa_3 = 145,\ 250,\ 460$ rpm compared with $\kappa_{sg} = 368$ rpm. The associated slope and saturation spectra are (**Figure 15**)

$$G_m(\kappa) = \frac{1}{2}\beta\kappa_2^{-1} = 10^{-4} \text{m}^2/\text{rpm}, \quad G_s(\kappa) = \kappa G_m(\kappa).$$

**Table 2  Pressure, elevation, slope, and saturation spectra (two-dimensional and one-dimensional) for the three components of gravity wave spectra, for $U = 10$ m s$^{-1}$.[1]**

| | Banner long gravity | | | | | Short gravity | | |
| --- | --- | --- | --- | --- | --- | --- | --- | --- |
| | vlg à la Phillips (1985) | | lg à la Phillips (1958) | | | sg Hwang (2005) | | |
| | $\omega_0, f_0$ | $n_{01}$ | $\omega_1, f_1$ | $n_{12}$ | $\omega_2, f_2$ | $n_{23}$ | $\omega_3, f_3$ | $n$ |
| | rps, Hz | | rps, Hz | | rps, Hz | | rps, Hz | |
| 1) $F_p(\omega_p)$ | 2.0, 0.32 | $-6$ | 5.0, 0.80 | $-7$ | 40, **6.4** | $-3$ | 100, 16 | $2N+3$ |
| 2) $F_\zeta(\omega_p)$ | **1.0**, 0.16 | $-4$ | 2.5, 0.40 | $-5$ | 20, 3.2 | $-3$ | 50, 8.0 | $N$ |
| | $\kappa_0, k_0$ | | $\kappa_1, k_1$ | | $\kappa_2, k_2$ | | $\kappa_3, k_3$ | $n$ |
| | rpm, cpm | | rpm, cpm | | rpm, cpm | | rpm, cpm | |
| 3) $F_\zeta(\kappa)$ | 0.10, 0.016 | $-3\frac{1}{2}$ | 0.63, **0.10** | $-4$ | 40, 6.4 | $-3$ | **250**, 40 | $\frac{1}{2}N - \frac{3}{2}$ |
| 4) $F_m(\kappa)$ | " | $-1\frac{1}{2}$ | " | $-2$ | " | $-1$ | " | $\frac{1}{2}N + \frac{1}{2}$ |
| 5) $G_m(\kappa)$ | " | $-\frac{1}{2}$ | " | $-1$ | " | $0$ | " | $\frac{1}{2}N + \frac{3}{2}$ |
| 6) $G_s(\kappa)$ | " | $+\frac{1}{2}$ | " | $0$ | " | $1$ | " | $\frac{1}{2}N + \frac{5}{2}$ |
| 7) $\beta^{-1} G_m(\kappa)$ | | $\frac{1}{2}\kappa_1^{-\frac{1}{2}}\kappa^{-\frac{1}{2}}$ | | $\frac{1}{2}\kappa^{-1}$ | | $\frac{1}{2}\kappa_2^{-1}\kappa^0$ | | |
| 8) $\beta^{-1}\langle m^2\rangle$ | | $1 - \left(\frac{\kappa_1}{\kappa_0}\right)^{-\frac{1}{2}}$ | | $\frac{1}{2}\ln\left(\frac{\kappa_2}{\kappa_1}\right)$ | | $\frac{1}{2}\left(-1 + \frac{\kappa_3(U)}{\kappa_2(U)}\right)$ | | |
| | | 0.60 | | 2.08 | | $-0.5+3.1$ | | |

[1]The four numbers underlying this table (bold, underlined) are chosen as follows: $\omega_0 = 1.0$ rps to give $U = C = g/\omega_0 = 10$ m s$^{-1}$, $k_1 = 0.10$ cpm from **Figure 10** (Banner 1990), $(\omega_p)_2 = 6.4$ Hz is based on W. Farrell & W.F. Munk (manuscript in preparation), and $\kappa_3 = 250$ rpm to agree with Bréon Henriot (BH) (ignoring capillaries). Adjoining numbers follow from $\omega = 2\pi f$, $\kappa = 2\pi k$, $\omega_p = 2\omega_1$, $\omega^2 = g\kappa$. Abbreviations: vlg, very long energetic gravity waves; lg, long gravity waves; sg, short gravities.

The slope spectra are white $[\neq f(\kappa)]$ and saturated $[\neq f(U)]$. Slopes grow with wind because of increasing band width.

**5.5.2. Banner–Bréon-Henriot reconciliation.** The BH measurements can be fitted to

$$10^3 \langle m^2 \rangle = a + bU \pm \varepsilon = 4 + 5.01\, U \pm 5.$$

The CM Hawaii measurements gave $3 + 5.12\, U \pm 4$. Because not all the world ocean is similar to the Alenuihaha Channel, we must attribute the results to response to local winds, only weakly dependent on fetch and other storm conditions.

There are four contributing components (**Table 2**):

(i) very long energetic gravity waves (vlg) that follow the Phillips (1985) $\kappa^{-3\frac{1}{2}}$ ($\omega^{-4}$) spectrum, between the wind-determined peak wavenumber $\kappa_0 = $ order .01 cpm and $\kappa_1 = $ order 0.1 cpm;

(ii) long gravity waves (lg) á la Phillips (1958) $\kappa^{-4}$ ($\omega^{-5}$) spectrum, from $\kappa_1$ to $\kappa_2 = $ order 10 cpm;

(iii) short gravities (sg) of undetermined spectral shape between $\kappa_2$ and the gc transition $\kappa_{gc} = 59$ cpm; and

(iv) capillaries with $\kappa > \kappa_{gc}$.

None of these components can be neglected. A principal difficulty is reconciling the lg logarithmic wind dependence to the linear BH relation. We could endow the ocean with antilogarithm capacity by setting $\kappa_2/\kappa_1 = e^{2bU}$, thus yielding a linear $bU$ relation for the lg, but this seems contrived.

Here we assume that each of the four components (and thus their sum) can be fit to an $a + bU \pm \varepsilon$ relation. We are fairly free to choose any $\kappa(U)$ to bring this about. I suggest that (i) and (ii) contribute largely to $a + \varepsilon$, whereas (iii) and (iv) are dominated by the $bU$ term.

For (i), we have $\langle m^2 \rangle = \beta(1 - \sqrt{\kappa_0/\kappa_1})$; setting $\kappa_0 = gU^{-2}$, we would need to assume $\kappa_1$ is proportional to $U^{-4}$ to make $\sqrt{\kappa_0/\kappa_1}$ proportional to $U$. A more likely situation is that $\langle m^2 \rangle = \beta(1 - \sqrt{\kappa_0/\kappa_1}) = 0.008(1 - 0.4) = 0.005$ (compared with a BH $= 0.004$) plus small wind-dependent terms. For (ii), by assuming the same wind dependence for $\kappa_1$ and $\kappa_2$ we can avoid the logarithmic problem and obtain $\langle m^2 \rangle = \log(\kappa_2/\kappa_1) = 2.3\beta = 0.016$. Using the values in **Table 2** for a 10 m s$^{-1}$ wind, we end up with $a = 0.017$ from the vlg and lg contributions, compared with BH $= 0.004$. Making acceptable adjustments to the above $\kappa$ limits can reduce $a$ from 0.017 to 0.010, which is still too large. The linear steepness relation remains an enigma.

## 6. SPREAD

The problem is to interpret the ratio of crosswind to downwind components of the BH mean-square slopes (Equation 9):

$$\langle m_y^2 \rangle / \langle m_x^2 \rangle = 0.73, \ 0.66, \ 0.62, \ 0.59 \quad \text{for} \quad U = 5, \ 10, \ 20, \ \infty \ \text{m/s} \tag{23}$$

(ratio 0.59 ignores the zero intercepts). The ratio is remarkably insensitive to wind speed, suggesting perhaps a geometric interpretation. An oil-covered surface (with reduced capillary contribution) has larger crosswind slope components than a surface not covered in oil (Cox & Munk 1956). Laboratory experiments give small crosswind slopes, as might be expected in narrow tanks (C. Cox & X. Zhang, manuscript in preparation). There is always the problem of wind gusts.

The underlying physics is not understood. At one time I expected the waves to be generated nearly along the wind direction; then why is the observed crosswind ratio so large? Some theoretical considerations suggest a predominant crosswind generation; then why is the ratio so small?

We start with a spectral decomposition.

$$\begin{pmatrix} \langle m_x^2 \rangle \\ \langle m_y^2 \rangle \\ \langle m^2 \rangle \end{pmatrix} = \int_0^\infty d\kappa \, G_\zeta(\kappa) \int_{-\pi}^{\pi} d\theta \begin{pmatrix} \cos^2 \theta \\ \sin^2 \theta \\ 1 \end{pmatrix} \phi(\kappa, \theta), \tag{24}$$

where $G_\zeta(\kappa)$ is the unidimensional spectrum of elevation $\zeta$, and $\phi$ is the directional spread function with $\int_{-\pi}^{\pi} \phi(\kappa, \theta) \, d\theta = 1$ (Appendix B). For definiteness I use the spread function (suppressing any dependence on $\kappa$)

$$\phi = \phi^+ + \phi^-, \quad \phi^\pm(\theta, \pm\theta_*, s) = \frac{\text{sech}^2(s(\theta \mp \theta_*))}{4s^{-1}\tanh(s\pi)}, \quad \int_{-\pi}^{\pi} \phi(\theta, \theta_*, s)d\theta = 1. \tag{25}$$

For isotropic radiation, $s = 0$ and $\phi = 1/2\pi$. The BH ratio $\langle m_y^2 \rangle / \langle m_x^2 \rangle = 0.66$ at $U = 10$ m s$^{-1}$ is consistent with a range of models, from a single broad beam ($\theta_* = 0$, $s = 0.89$) to two pencil beams ($\theta_* = \pm39°$, $s = \infty$), (**Figure 16**, **Table 3**). The former case has half-power points at exactly $\theta = \pm 1$ radian. I take this value as representative for the single broad beam model.

Perhaps the simplest model is one where wave components in the direction $\theta$ respond to the wind projection along the wave direction: $\phi(\theta) \sim \cos\theta$. Evaluating the integral (Equation 24) leads to $\langle m_y^2 \rangle / \langle m_x^2 \rangle = \frac{1}{2}$ as compared with the BH ratio 0.66.

A lower limit on the width of the spreading functions comes from the pressure fluctuations at depths that are large compared with wave length (Section 5.4). This phenomenon requires some oppositely traveling wave energy, which leads to a standing-wave component of the deep pressure
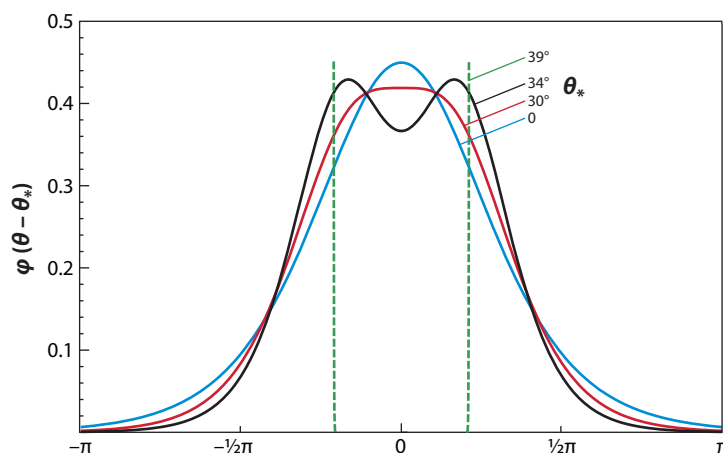
**Figure 16**

The spread function for stated values of $\theta_*$, all consistent with a Bréon Henriot (BH) ratio of 0.66. $\theta_* = 0$ consists of a single broad beam centered in the wind direction; $\theta_* = 39°$, $I = 0$ consists of two pencil beams at $\pm 39°$. The beam is a maximum along the wind direction for $\theta_* < 30°$, $I > 0.056$ and a minimum for $\theta_* > 30°$, $I < 0.056$.

field. The method has previously been used to estimate the reflection of ocean swell at the coastline (Haubrich et al. 1963) and the directional wave pattern of 7 s waves (Tyler et al. 1974).

We define the spread overlap function and its integral as follows:

$$\Phi(\theta, s) = \phi(\theta, s)\phi(\pi - \theta, s), \quad I(s) = \int_{-\pi}^{\pi} \Phi(\theta, s)\, d\theta$$

(see **Supplemental Figure 2**). **Table 3** lists the spread integral for various spread functions.

The spread integral can vary from 0 (no overlap) to $1/(2\pi) = 0.16$ (isotropic radiation). In principle the spread integral can be determined from Equation 22 given accurate information of the quantitites on both sides of the equation, and this could furnish useful limits to the directional spread of the surface waves (W. Farrell & W.H. Munk, manuscript submitted).

Can we get some guidance from models of wave generation? I believe we can, and I believe that these models favor a bimodal spread function. Here I distinguish one-dimensional (long-crested) waves, such as those generated by broad paddles in wave tanks, from the two-dimensional waves of length comparable to or longer than the generator (such as ship waves). In the former case, the long-crested waves are subject to Benjamin & Feir instability, which eventually transforms the waves into a two-dimensional pattern (for example, Zakharov & Rubenchik 1973; see Yuen & Lake 1980 for a general review). It has been suggested that the BH ratio has its roots in a Benjamin & Feir instability.

**Table 3    Spread parameters**

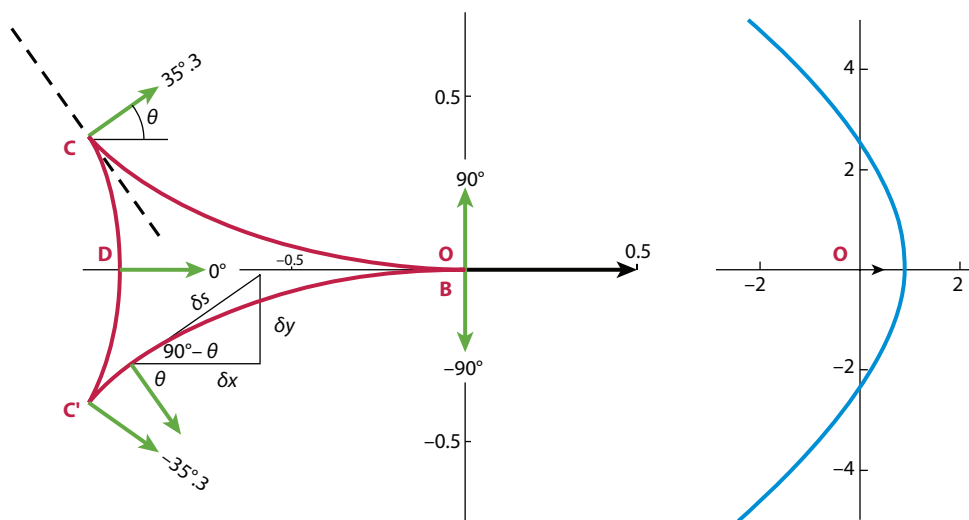| $\theta_*$ | isotropic | 0 | 30° | 34° | 39° |
|---|---|---|---|---|---|
| $s$ | 0 | 0.89 | 1.25 | 1.56 | $\infty$ |
| $I(s)$ | $1/2\pi$ | 0.098 | 0.056 | 0.031 | 0 |
| $\langle m_y^2 \rangle / \langle m_x^2 \rangle$ | 1 | 0.66 | 0.66 | 0.66 | 0.66 |

**Figure 17**

Ship wake by a pressure point **O** traveling in the positive x direction, for gravity only (*left*) and surface tension only (*right*). The full wake consists of many such wake elements (**Figure 18a** shows $n = 1$ and $n = 2$). Wave direction is normal to the wake crest in direction $\theta$ relative to the course of the moving pressure point. The gravity wake consists of transverse (stern) wave **C D C′** and the divergent (bow) waves **B C** and **B C′**. Point **D** at the center of the stern wave travels in the ship direction ($\theta = 0°$). At the bow B the divergent wave travels normal ($\theta = 90°$) to the ship's course. At the prominent caustic (the cusp C), where the bow and stern waves coalesce, $\theta = 35°.3$ independent of the ship speed (but see **Figure 18**). The gravity wake is entirely behind the pressure point, whereas some of the capillary wake is forward of **O**.

## 6.1. Ship Wake

The simplest example is that of the two-dimensional wave pattern caused by a pressure point traveling at constant velocity $C$ over the sea surface. The wake pattern consists of two components (**Figure 17**): stern waves that travel in the general direction of the ship's course and bow waves that travel at a large angle relative to the course. At the bow (where the waves are most prominent) the waves travel at a right angle! I have found this example to be a simple way to come to terms with the large cross-wind slope component.

Here I follow the discussion in Lamb (1932, para. 256); this discussion goes back to Lamb's own work in 1922 and to *Popular Lectures* on ship waves by Sir W. Thomson (Lord Kelvin) in 1887. Generation at the gc transition necessarily involves microships (not microchips), with surface tension playing an important role.

**6.1.1. Dispersion.** The phase velocities of pure gravity waves ($T' = 0$) and pure capillaries ($g = 0$) are given by

$$C_g^2(\kappa) = g/\kappa \quad \text{and} \quad C_c^2(\kappa) = T'\kappa, \tag{26}$$

respectively. It can be shown that for combined gravity and surface tension

$$C^2 = C_g^2 + C_c^2 \tag{27}$$

with a minimum at the gc transition

$$C_{gc} = (4g\,T')^{\frac{1}{4}} \quad \text{at} \quad \kappa_{gc} = (g/T')^{\frac{1}{2}}. \tag{28}$$

**6.1.2. Ship wake and fishline.** Lamb (1932, pp. 433 and 469) gives a geometric construction of a ship wake $Y(X)$ in terms of a length parameter $p(\theta)$

$$-X = p \cos \theta - p' \sin \theta, \quad Y = p \sin \theta + p' \cos \theta, \quad p' = dp/d\theta \tag{29}$$

$$dY/dX = \cot \theta,$$

with[6]

$$+p_g = \lambda_g \cos^2 \theta, \quad \lambda_g = 2\pi g^{-1} V^2 \tag{30}$$

$$-p_c = \lambda_c \cos^{-2} \theta, \quad \lambda_c = 2\pi T' V^{-2} \tag{31}$$

for gravity and capillary waves, respectively (**Figure 17**), where $V$ is the ship speed made stationary by a superposed current $-V$ and $\lambda_g$, $\lambda_c$ are the wave lengths in deep water of pure gravity and capillary waves with phase velocity $C$.

**6.1.3. Combined gravity and surface tension.** For the combined problem, the wake is given by (Lamb 1932, p. 469, eq. 9)

$$p^\pm(\theta, \alpha) = \pm \frac{1}{2} \lambda_g (\cos^2 \theta \pm \sqrt{\cos^4 \theta - \cos^4 \alpha}), \quad \theta \le \alpha \tag{32}$$

$$\cos \alpha = C_{gc}/V. \tag{33}$$

For both the limits $T' \to 0$ and $g \to 0$, we have $C_{gc} \to 0$, $\cos \alpha \to 0$, and so

$$p^+ \to \lambda_g \cos^2 \theta = p_g$$

$$p^- \to -\frac{1}{2} \lambda_g \cos^2 \theta \, \frac{1}{2} \cos^4 \alpha / \cos^4 \theta$$

$$= -\frac{1}{4} \lambda_g \cos^{-2} \theta \, \cos^4 \alpha = -\lambda_c \cos^{-2} \theta = +p_c,$$

in agreement with Equations 30 and 31. These are the only $Y(X)$ wake profiles independent of $V$ (other than for the scale factors $\lambda$). Further, as

$$V \to \infty, \quad p^+ \to p_g, \quad p^- \to p_c \to 0$$

$$V \to C_{gc}, \quad \theta \to 0, \quad dY/dX \to \infty, \quad p^- \ne p_c.$$

Thus, the limits $V \to \infty$ and $T' \to 0$ are equivalent, but $V \to C_{gc}$ and $g \to 0$ are not equivalent.

**Figure 18** shows the transition from gravity to capillary waves with increasing $V$ [**Figure 18b** and **e** are for the parameters used by Lamb 1932 (p. 470)]. Red and blue lines correspond to $p^\pm$. The second wake front (out of an infinite number) is shown only for **Figure 18a** and **e** ($n = 2$). In general there are four cusps ($B$, $B'$, $C$, $C'$); $C$ and $C'$ coalesce at the source ($X$, $Y = 0$) for pure gravity waves (1a); $BC$ and $B'C'$ are the bow wakes and $CC'$ is the stern wake. With decreasing $V$ the cusp $B$ recedes and connects to the red gravitational Mach stem (**Figure 17c**), paralleling an independent blue capillary Mach stem. At a critical source speed $V = 1.94 \, C_{gc}$ the gravitational cusps collapse. With further decrease of $V$ the forward points of the stems become rounded and for the capillary wakes outrun the source. In the limit $V = C_{gc}$ the wakes form straight lines normal to the ship's course, forward of the source for the capillaries, behind the source for the gravity waves, in accordance with group velocity $U_c > V$ and $U_g < V$.

---

[6]In the classical literature the ship travels in the $-x$ direction, held stationary by a superposed current $+V$. The sign for $p_g$ ($p_c$) is associated with group velocity $U_g < C_g$ ($U_c > C_c$). (Lamb 1932, footnote p. 469)
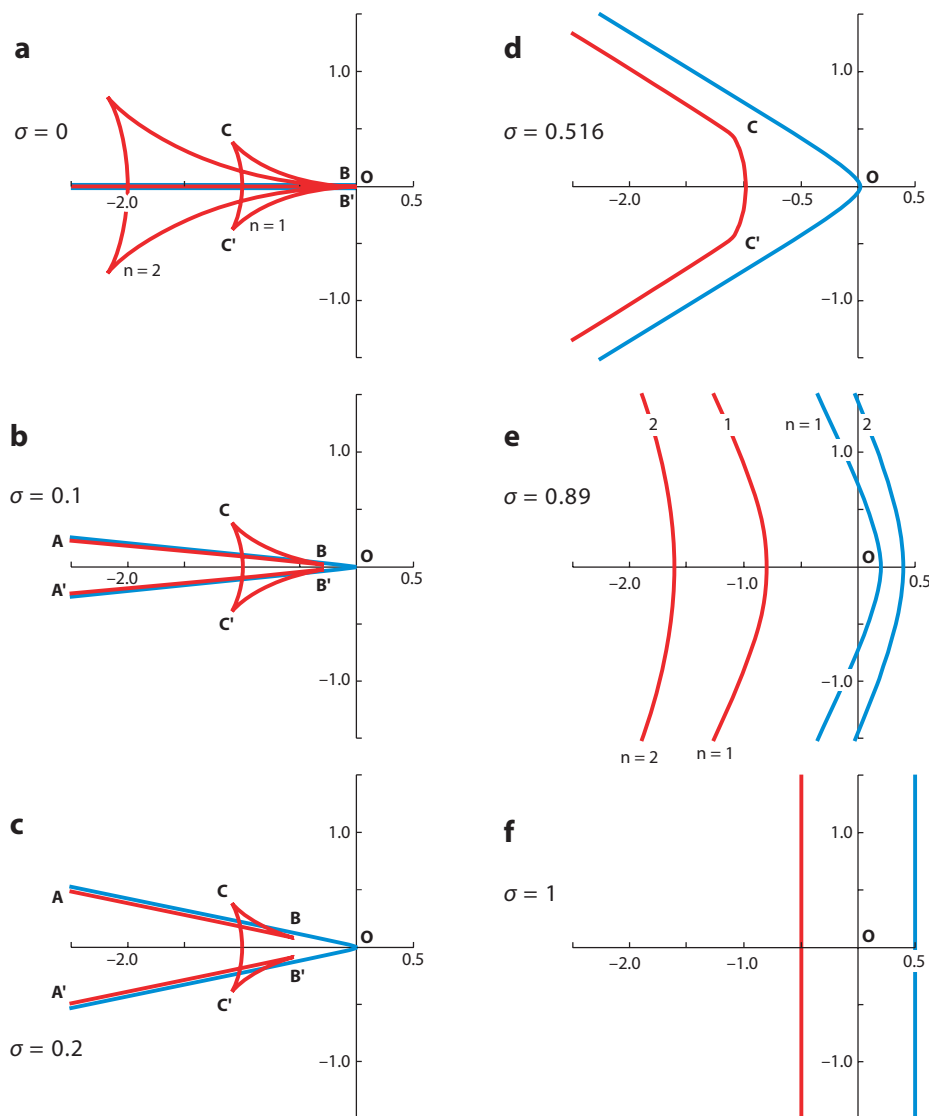
**Figure 18**

Ship wake element for combined gravity and surface tension, showing gravity waves modified by surface tension (*red*) and capillaries modified by gravity (*blue*). For $\sigma = C_{gc}/V \ll 1$, the quasi-gravity waves are unchanged from **Figure 17**; capillaries form an infinitely sharp Mach stem. With increasing $\sigma$ the Mach stem **A O A′** opens and the crest points **B** and **B′** split and fall behind the source **O** so that the divergent wave crests **B C** and **B′ C′** shrink. For the critical case (*d*), $\sigma = 0.516$ and $V = 0.45$ m s$^{-1}$, the divergent waves disappear and are replaced by double caustics **C** and **C′**. There is no wake signature for $V < C_g$.

**Figure 18*a–f*** is drawn for the general solution $p^{\pm}(V)$ with decreasing $V$. **Figure 17** shows the solution for gravity waves $p(g, \ T' \to 0)$ only and for capillary waves $p(g \to 0, \ T')$ only. The former coincides with the $p^+(V \to \infty)$ limit, but the latter differs from the $p^-(V \to C_{gc})$ limit.

**6.1.4. Double caustic.** The model generation consists of multiple pulses along the path, each radiating uniformly in all directions. Let $dS$ be the incremental distance along the wake front. Regions of small $S' = dS/d\theta$ are intense, they represent a broad range of radiated angles focused into a narrow wake segment. From Equation 29,

$$X' = (p + p'')\sin\theta, \quad Y' = (p + p'')\cos\theta$$
$$S' = \sqrt{X'^2 + Y'^2} = \pm(p + p'') \equiv \pm P(\theta). \tag{34}$$

The prominent cusps are associated with vanishing $P$. For pure gravity and pure capillary waves,

$$P_g \sim 3\,\sin^2\theta - 1, \quad P_c \sim \sec^2\theta(1 + 2\,\sec^2\theta + 4\,\tan^2\theta).$$

For the gravity waves, $P_g = 0$ gives the classical cusp at $\theta = \sin^{-1}\sqrt{(1/3)} = 35°.3$; there is no corresponding feature $P_c = 0$ for capillary waves. For the general case (Equation 32) we have $P(\theta, \alpha) = 0$ yielding a caustic along $\alpha_c(\theta)$ and a double caustic $\alpha_{cc}$, $\theta_{cc}$ for $d\alpha_c/d\theta = 0$.

**Figure 19** shows the contours[7] $P^\pm(\theta, \alpha) = -1, 0, +1$. The $P^+ = 0$ contour is a locus of caustic enhancement. There is no $P^- = 0$ contour, hence there is no capillary caustic. The traditional gravity wave wake (Equation 29) is associated with $\alpha = \pi/2$, hence $V/C_{gc} = \infty$. Here the $P^+ = 0$ contour has two intersections: $\theta = 35°.3$ and $\theta = 90°$; these can be associated with the traditional C caustics and the bow caustic B (**Figure 17**). I consider the case $V/C_{gc} = 5$ in detail. The A caustic is now associated with a slightly increased $\theta$, and the B caustic has split in two and fallen behind the bow. The bow wake between B and C has shortened.

The critical case is for

$$\left.\begin{array}{l} \alpha = 1.029, \quad \sec\alpha = 1.938, \quad \theta = 0.767\,\text{rad} = 43°.9 \\ V = 1.938\,C_{gc} = 0.447\,\text{m/s}, \quad \lambda = 7.38\,\lambda_{gc} = 0.126\,\text{m}, \quad f = 3.55\,\text{Hz} \end{array}\right\} \tag{35}$$

where $\lambda(C)$ and $f(C)$ follow from gc dispersion for $C = V$. The bow wake has collapsed; there is no traditional triangular wake for $V < 0.447\,\text{m s}^{-1}$. The value $\theta = 43.9°$ is not far from $\theta_* = 39°$ deduced from the BH ratio 0.66 for two narrow pencil beams. I surmise that the dimensions (Equation 35) are an important element in the gc transition.

**6.1.5. The slope of ship wakes.** I have not been able to reproduce Lamb's (1932, p. 436, eq. 16) amplitude factor[8]. The first term is

$$A_{Lamb} = \sqrt{\frac{2g}{\pi\lambda_g}}\,\frac{P_0}{\rho V^3} = \frac{g}{\pi\rho}\,P_0\,V^{-4}.$$

(Clearly the wake amplitude does not go to infinity as $V \to 0$.) Now write

$$P_0 = K\rho V^2 \text{area} \times f(V/V_{crit}), \quad K \text{ dimensionless constant}$$
$$A_{Lamb} = \pi^{-1}Kg V^{-2}\,\text{area} \times f(V/V_{crit})$$

where $V_{crit}$ refers to (Equation 31). The associated slope amplitude for stern waves of length $\lambda_g$ is

$$m = \frac{2\pi A}{\lambda_g} = \pi^{-1}Kg^2 V^{-4}\,\text{area} \times f(V/V_{crit}) = 4\pi K\lambda^{-2}\text{area} \times f(V/V_{crit}).$$

---

[7]The analytic expressions for $P^\pm(\theta, \alpha)$ are complex and not reproduced here.

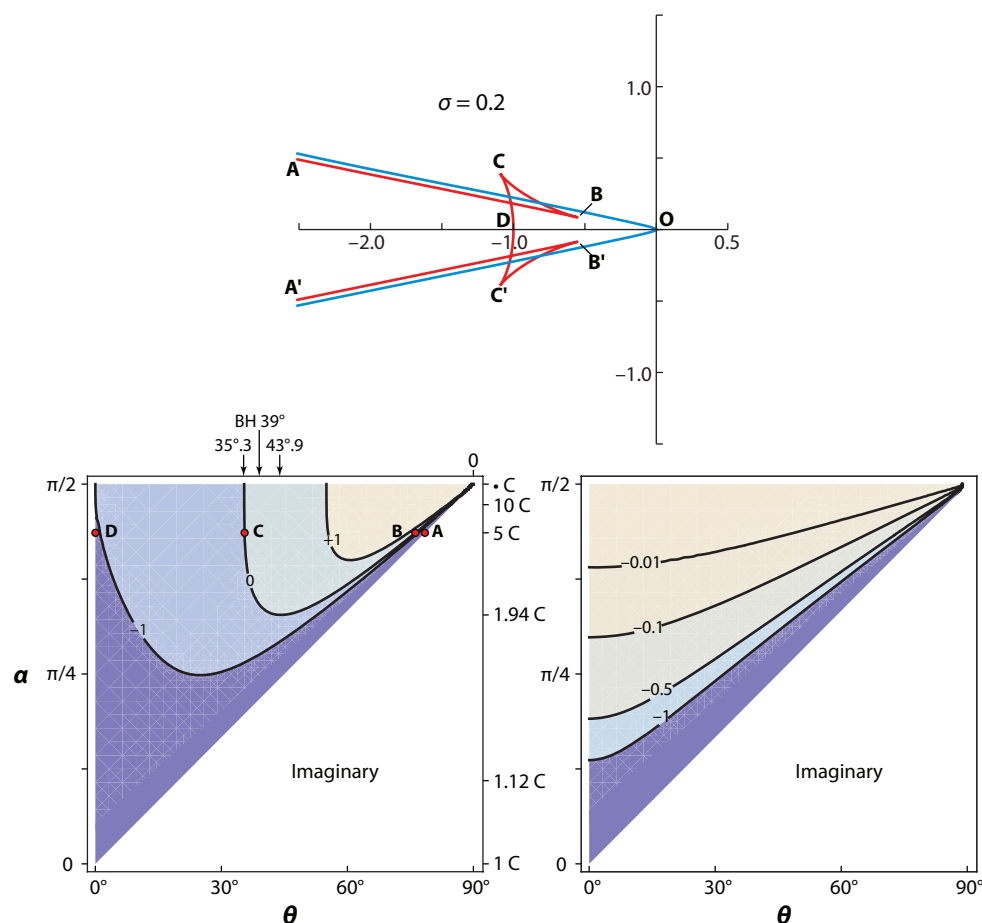[8]Lamb's $c$ is ship speed (my $V$), and his $a$ is the wavelength $\lambda_g = 2\pi V^2/g$ (see Lamb 1932, p. 434, eq. 6).

**Figure 19**

Contour diagrams of the dispersion parameter $P^{\pm(\theta,\,\alpha)}$, where $\theta$ is the wave direction and $\alpha = C_{gc}/V$. $P^+ = 0$ (*left*) is associated with intensive caustics in gravity-controlled wakes (modified by surface tension). There are no $P^- = 0$ contours (*right*) for surface tension–controlled wakes. The lowest point in the $P^+ = 0$ contour at $V = 1.94C_m$ corresponds to the wake transition (**Figure 18d**). The $P^+ = 0$ contour intersects at $\alpha = 90°$ at two points: **O** bow waves at the source and 35°.3 the cusp of the traditional gravity wake. The Bréon-Henriot (BH) ratio $\langle m_y^2 \rangle/\langle m_x^2 \rangle = 0.66$ corresponds to $\theta = 39°$ (42° for oil-covered surfaces). The upper sketch, showing gravity-controlled (*red*) and surface tension–controlled (*blue*) wakes is reproduced for identification of the principal features.

For the intensive caustic waves, the length is shorter, and the slope is larger by a factor $\sec\theta_{cusp}$. Now suppose the area of the pressure spot is $b^2\lambda^2$. Then the slope amplitude is

$$m = 4\pi K b^2 \, \sec\theta_{cusp} \, f(V/V_{crit}). \tag{36}$$

For the special case $f(V/V_{crit}) = \sqrt{V/V_{crit}}$, the mean-square slope $\frac{1}{2}m^2$ grows linearly with ship velocity $V$ according to

$$\langle m^2 \rangle = \frac{1}{2}(4\pi K b^2 \, \sec\theta_{crit})^2 V/V_{crit}. \tag{37}$$

**6.1.6. Is there a BH connection?** Thus for a pressure spot of area $b^2 \lambda_g^2$ and magnitude $K \rho V^2 \sqrt{V/V_{crit}}$ moving along the surface with velocity $V$ we can reproduce the BH linear dependence $\langle m^2 \rangle = 5 \times 10^{-3} U$ provided

$$
\begin{aligned}
5 \times 10^{-3} &= \frac{1}{2} (4\pi K b^2)^2 \ \sec^2 \theta_{crit} / V_{crit} \\
&= 340 (K b^2)^2
\end{aligned}
$$

or $K b^2 = 0.0038$. None of this is impossible.

**6.1.7. Phillips resonance.** We related the singularity (Equation 35) to a Phillips resonance. For a classical logarithmic wind profile we have

$$
U(U_{10}, \ \lambda_{crit}/2\pi) \cos \theta_{crit} = V_{crit},
$$

which yields $U_{10} = 1.02$ m s$^{-1}$. This is the lowest wind speed for generating the double caustic.

**6.1.8. Conclusion.** The BH statistics impose restrictions on the spread function of short gravity waves; the spread function is consistent with models that range from a single broad (one-radian-wide) beam directed downwind to two narrow beams directed 39° to the left and right of the wind. Microseismic evidence places a lower limit on beam width. Generation models of the ship-wave type favor a bimodal spread function and are not inconsistent with the 0.66 BH ratio. I have ignored the directional spread of wind gusts.

## 7. SKEWNESS

The sudden emergence of skewness at winds $U > 2$ m s$^{-1}$ and saturation above 6 m s$^{-1}$ are lead features of the BH statistics. I find it convenient to refer to dimensionless parameters $\alpha = \kappa a$ and $\beta = \kappa b$, where $\kappa$ is the wavenumber in radians per meter and $a, b$ are the crest coordinates in a coordinate system centered at the mean sea level midway between two adjoining troughs (**Figure 20**). For the traditional Stokes wave $\beta = 0$.
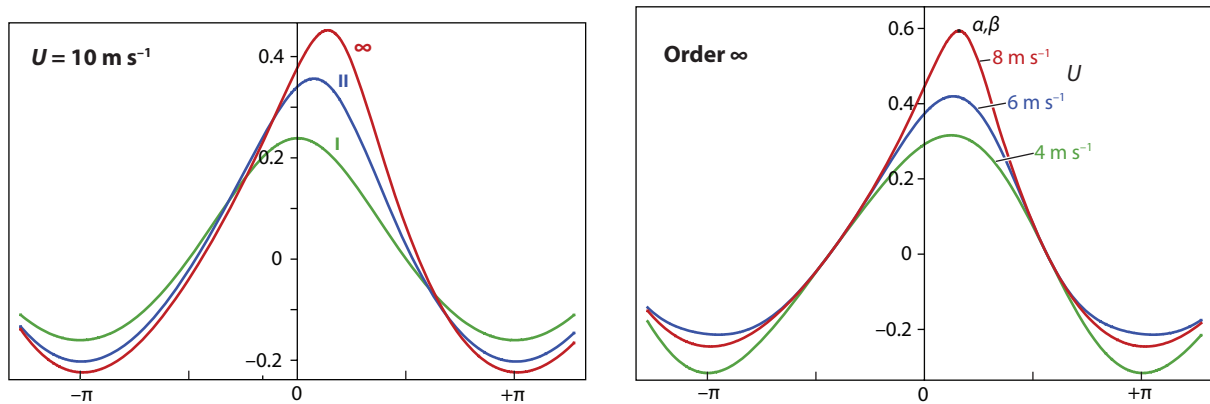


**Figure 20**

(*a*) Wave profiles to orders I, II, $\infty$ for $\langle m^2 \rangle = 0.05$, corresponding to wind speed of 10 m s$^{-1}$. (*b*) Wave profiles to order $\infty$ for $\langle m^2 \rangle = 0.02, \ 0.04, \ 0.06$, corresponding to wind speeds of 4, 6, 8 m s$^{-1}$.

## 7.1. One-Scale Model

A simple interpretation is in terms of Stokes waves with skewness introduced by a phase-shifted bound second harmonic (see **Supplemental Appendix 2**). In free waves, such a phase-shifted harmonic can occur only in a transient state.

Following the classical Stokes-Rayleigh expansion for irrotational waves in deep, incompressible water, made stationary by an opposing current, write

$$y_s = ae^{ky_s} \cos kx - be^{2ky_s} \sin 2kx = y_s^I + \cdots \tag{38}$$

for the surface elevation above the undisturbed level, with a skewness term of amplitude $b$. Expanding the exponential leads to $y^I(x) = a \cos kx - b \sin 2kx$, $y^{II}(x)$, ...; a numerical solution of the "exact" Equation 38 is designated $y^\infty(x)$. Crests are delayed relative to the troughs by

$$\beta = -4b/a \tag{39}$$

(**Figure 20**). Differentiation leads to expressions for the slopes $m^I(x)$, $m^{II}(x)$, $m^\infty(x)$, with moments

$$\langle m^2 \rangle = \frac{1}{2\pi} \int_{-\pi}^{\pi} dx\, m^2(x), \quad \langle m^3 \rangle = \frac{1}{2\pi} \int_{-\pi}^{\pi} dx\, m^3(x), \quad \langle m^3 \rangle_{norm} = \langle m^3 \rangle / \langle m^2 \rangle^{3/2},$$

$$\left.\begin{array}{l} \langle m^2 \rangle = f_1(\alpha, \beta) = \frac{1}{2}\alpha^2 + \frac{1}{2}\alpha^4 + \frac{11}{32}\alpha^2\beta^2 + \cdots \\ \langle m^3 \rangle_{norm} = f_2(\alpha, \beta) = -3 \times 2^{-\frac{3}{2}}\beta - 3 \times 2^{\frac{1}{2}}\alpha\beta + \cdots \end{array}\right\} \tag{40}$$

to first and second order. Each point of the BH relation in **Figure 7** gives a value of $\langle m^2 \rangle_{BH}$ and $\langle m^3 \rangle_{norm,\,BH}$ and the solution to the two equations,

$$\langle m^2 \rangle_{BH} = f_1(\alpha, \beta), \quad \langle m^3 \rangle_{norm,BH} = f_2(\alpha, \beta),$$

can be solved for the two unknowns $\alpha$, $\beta$. The 31 BH values then determine $\beta(\alpha)$ (**Table 4**, **Figure 21**). To first order $\alpha^I = \sqrt{2\langle m^2 \rangle}$ and $\beta^I = \frac{1}{3}2^{\frac{3}{2}}\langle m^3 \rangle$. To the second order there is some cross talk, and $\alpha^\infty, \beta^\infty$ need to be solved for numerically by going back to Equation 38. The fractional correction of $\langle m^2 \rangle$ for $\beta$ is only 3% at saturation. Hence, skewness and steepness are sufficiently orthogonal so that the sharp increase in skewness can occur without disturbing the linearity in the steepness relation to wind speed.

The step-like dependence of $\beta^\infty(\alpha^\infty)$ implied by the BH statistics is astounding. One is tempted to write

$$\beta = 0 \quad \text{for} \quad \alpha \le \alpha_{crit}, \quad \beta = \alpha \quad \text{for} \quad \alpha = \alpha_{crit} = 0.3. \tag{41}$$

**Table 4   Steepness and skewness parameters to first, second and infinite order, as derived from the BH statistics**

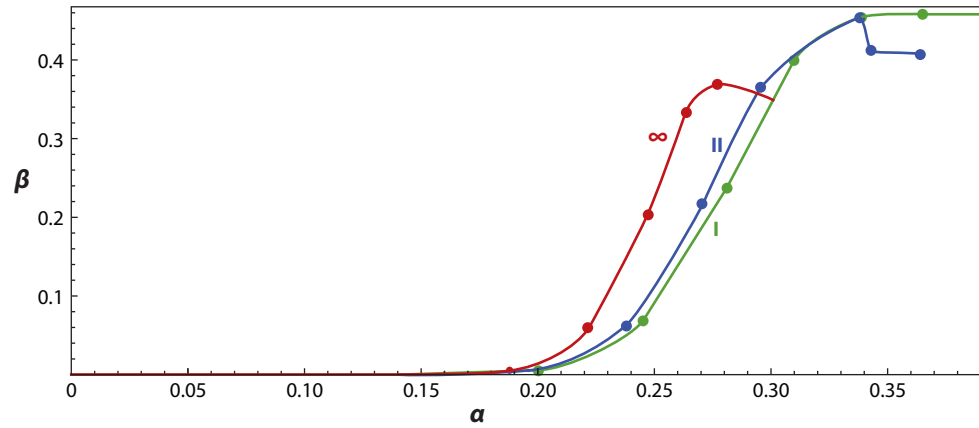| $\langle m^2 \rangle$ | $\langle m^3 \rangle_{norm}$ | $\alpha^I$ | $\beta^I$ | $\alpha^{II}$ | $\beta^{II}$ | $\alpha^\infty$ | $\beta^\infty$ |
|---|---|---|---|---|---|---|---|
| 0.01 | $-2.7 \times 10^{-5}$ | 0.141 | $-2.6 \times 10^{-5}$ | 0.140 | $-2.5 \times 10^{-5}$ | 0.140 | $-2.4 \times 10^{-5}$ |
| 0.02 | $-5.9 \times 10^{-3}$ | 0.200 | $-5.6 \times 10^{-3}$ | 0.196 | $-5.3 \times 10^{-3}$ | 0.188 | $-5.2 \times 10^{-3}$ |
| 0.03 | $-0.072$ | 0.245 | 0.068 | 0.238 | 0.063 | 0.222 | 0.060 |
| 0.04 | $-0.247$ | 0.281 | 0.237 | 0.271 | 0.217 | 0.247 | 0.203 |
| 0.05 | $-0.400$ | 0.310 | 0.400 | 0.296 | 0.366 | 0.263 | 0.330 |
| 0.06 | $-0.447$ | 0.338 | 0.454 | 0.338 | 0.454 | 0.277 | 0.369 |
| 0.07 | $-0.450$ | 0.365 | 0.458 | 0.343 | 0.412 | 0.29 | 0.358 |
| 0.08 | $-0.450$ | 0.390 | 0.458 | 0.364 | 0.408 | 0.301 | 0.349 |

**Figure 21**

Function $\beta(\alpha)$ evaluated from BH statistics to order I, II, $\infty$.

Two points are to be noted: (*a*) The transition steepness $\alpha_{crit}$ corresponds to Longuet-Higgins (1995) extreme wave of $\alpha = 0.301$, and (*b*) for $\alpha > \alpha_{crit}$ the crest spills forward by an amount roughly equal to the crest elevation.[9]

## 7.2. Two-Scale Model

The previous discussion of a one-scale model (the short gravity waves) has limited applicability. Significant skewness and breaking do not occur until the steepness exceeds 0.2; at this stage waves crests have sharpened, and there is considerable energy flux into parasitic capillaries. For any meaningful appraisal one must consider at least the two scales to both sides of the gc transition.

C. Cox (personal communication) has attributed skewness to simple slope addition. Ignoring the two-dimensional aspects, elevation and slope are given by

$$\zeta(x) = a_g \cos(\kappa_g x + \varepsilon_g) + H(x)\alpha_c \cos(\kappa_c x + \varepsilon_c)$$
$$m(x) = -\alpha_g \sin(\kappa_g x + \varepsilon_g) - H(x)\alpha_c \sin(\kappa_c x + \varepsilon_c), \tag{42}$$

with $\alpha = k\,a$ and

$$H(x) = 1 \text{ for } 0 < \kappa_g\,x < \frac{1}{2}\pi$$

and zero elsewhere (parasitic waves on forward quarter of wave). We introduce two crucial ratios:

$$n = \kappa_c/\kappa_g, \quad r = (\alpha_c/\alpha_g) \text{ for } 0 < \kappa_g x < \frac{1}{2}\pi \tag{43}$$

and zero elsewhere. The slope moments are

$$M_j \equiv \langle m^j \rangle = -\alpha_g^j \frac{1}{2\pi} \left[ \int_0^{\pi/2} dx [\sin(\kappa_g x + \varepsilon_g) + r\,\sin(\kappa_c x + \varepsilon_c)]^j + \int_{\pi/2}^{2\pi} dx [\sin(\kappa_g x + \varepsilon_g)]^j \right].$$

---

[9]The reader is reminded that the first order slope amplitude $\alpha$ is of the same order as the elevation of the crest above the mean level (in units $1/\kappa$). For example, $y_{crest} - \bar{y} = 0.1,\ 0.2,\ 0.3$ for $\alpha = 0.1,\ 0.18,\ 0.24$ (Longuet-Higgins 1995).

For $n \gg 1$,

$$\langle m \rangle = 0$$
$$\langle m^2 \rangle = \alpha_g^2 \, f^{II}, \quad f^{II} = \tfrac{1}{2} + \tfrac{1}{8} r^2$$
$$\langle m^3 \rangle = \alpha_g^3 \, f^{III}, \quad f^{III} = -\tfrac{3}{4\pi} r^2$$
$$\langle m^4 \rangle = \alpha_g^4 \, f^{IV}, \quad f^{IV} = \tfrac{3}{32} + \tfrac{3}{8} r^2 + \tfrac{3}{8} r^4.$$
$$\langle m^3 \rangle_{norm} = f^{III}/(f^{II})^{3/2}, \quad \langle m^4 \rangle_{norm} = f^{IV}/(f^{II})^2 - \tfrac{3}{8}.$$

The normalized mean cube has a maximum (negative) value of

$$\max(\langle m^3 \rangle_{norm}) = -4\sqrt{2/3} \, \pi^{-1} = -1.04 \text{ for } r = \sqrt{8}.$$

**7.2.1. Mean squares.** We can get some rough estimates for $r$ and $n$ from the CZ experiments (**Table 5**). The modifications of $r$ by the cross terms are negligible. As expected, with increasing wind and fetch, $\langle m^2 \rangle$ increases, $f_g$ decreases, and $f_c$ and $n$ increase; the gc gap widens. However, the relative capillary slope amplitude $r$ appears to saturate at moderate and high winds. Some paddle-driven runs have much weaker capillaries, perhaps indicating a direct wind input. The cross-paddle component is negligible.

Glitter-derived variance statistics have no information on relative contributions from gravity and capillary waves. The limited experience from the CM slick measurements is consistent with the previous finding that gravity and capillary wave contributions are comparable ($r = $ order 1) at moderate and high winds.

**7.2.2. Mean-cube and mean-fourth.** We can now examine the consequences of the Cox model of ascribing the BH statistics to the addition of gravity wave and capillary slopes. For each point of the BH relation $\langle m^3 \rangle_{norm} = f_{BH}(\langle m^2 \rangle)$ we have two equations:

$$\langle m^2 \rangle = \alpha_g^2 \, f^{II}(r), \quad \langle m^3 \rangle_{norm} = \frac{f^{III}(r)}{[f^{II}(r)]^{3/2}},$$

which can be solved for $r$ and $\alpha_g$. The assembly of points yields $r(\alpha_g)$ (see **Supplemental Figure 3**).

I can now plot various parameters as functions of $\langle m^2 \rangle$, given the Cox Zhang sum hypothesis (see **Supplemental Figure 4**). The agreement of $\langle m^3 \rangle$ with the glitter data does not give any comfort, it just confirms the above curve fitting. There may be some support in the precipitous

**Table 5** Cox-Zhang laboratory slope spectra for various wind speeds and fetches. Numbers (…) correspond to parasitic resonance: $C_c = C_g$. Orbital smearing produces a broadened flat peak with center frequency somewhat lower than (…)

| $U$ (m s$^{-1}$) | 3.5 | 4.4 | 5.2 | 6.1 | 5.2 | 6.1 |
|---|---|---|---|---|---|---|
| $F$ (m) | 2.8 | 2.8 | 2.8 | 2.8 | 2.3 | 2.0 |
| $f_g$ (Hz) | 6.1 | 4.8 | 4.6 | 3.8 | 5.0 | 4.6 |
| $f_c$ (Hz) | 63 (47) | 83 (84) | 92 (94) | 97 (159) | 85 (76) | 82 (94) |
| $n$ | 10 (8) | 17 (18) | 20 (20) | 26 (42) | 17 (15) | 18 (20) |
| $\langle m^2 \rangle$ | 0.021 | 0.045 | 0.048 | 0.056 | 0.048 | 0.063 |
| $\langle m_c^2 \rangle / \langle m^2 \rangle$ | 0.29 | 0.41 | 0.42 | 0.42 | 0.49 | 0.49 |
| $r_{approx}$ | 1.08 | 1.28 | 1.30 | 1.30 | 1.40 | 1.40 |
| $r_{exact}$ | 1.06 | 1.26 | 1.28 | 1.28 | 1.38 | 1.38 |

rise of $\langle m^4 \rangle$:

$$\langle m^4 \rangle_{norm} \text{ from 0.1 to 0.5 for } \langle m^2 \rangle \text{ from 0.03 to 0.05}$$

(see **Supplemental Figure 3**);

$$\langle m^4 \rangle_{norm} \text{ from 0.2 to 0.6 for } \langle m^2 \rangle \text{ from 0.15 to 0.035}$$

(see **Figure 4**).

But other features in the fourth moment show no resemblance. We previously noted that a saturation of $r = $ order 1 for $\langle m^2 \rangle > 0.04$ is consistent with the laboratory spectra. However, the overall evidence is not convincing.

The sharp rise of $r(\alpha_g)$ between $\alpha_g = 0.2$ and $0.3$ (see **Supplemental Figure 3**) resembles the precipitous rise of $\beta(\alpha)$ between $\alpha = 0.2$ and $0.25$ (**Figure 20**). As always, we need to account for the surprising linearity of $\langle m^2 \rangle = a + bU$ in the presence of the precipitous changes in the third moment of the slope distribution. For the one-scale model the explanation appears to be the near-orthogonality of skewness $\beta$ with steepness $\alpha$. For the parasitic two-scale model this explanation is no longer available, because $r = \alpha_c/\alpha_g$ is a direct contribution to the overall slope distribution. Thus, whereas one might account for skewness by the uneven distribution of the capillaries on the forward slope of the steep gravities, one would expect them to show up as a significant enhancement in mean-square slope. This is not the case.

**7.2.3. Capillary dissipation and drag.** The total energy per unit area of capillary waves is (Lamb 1932, section 266.19)

$$E = \frac{1}{2}\rho_w \kappa C^2 a_c^2.$$

The modulus of decay due to viscosity is

$$\dot{E}/E = 2\nu\kappa^2, \qquad \frac{1}{4}\sqrt{2}\,\nu^{\frac{1}{2}}C^{\frac{1}{2}}\kappa^{\frac{3}{2}}$$

for clean and dirty water (Lamb 1932, section 351). Finally, $\tau = \dot{E}/C$. Putting all this together, we have

$$\tau = 4\nu\rho_w\kappa C\sigma^2 = \tau_0 \gamma K \alpha_c^2$$
$$\tau_0 = \rho_w C_m^2 = 53 \text{ N/m}^2$$
$$\gamma = \frac{\nu\kappa_m}{C_m} = \left(\frac{\nu^4 g}{4T^{13}}\right)^{1/4} = 1.6 \times 10^{-3} \text{ (dimensionless)}$$
$$K(\kappa) = 2\kappa_c C_c = 2\kappa_c\sqrt{\frac{1}{2}(\kappa + \kappa^{-1})} = \sqrt{2(n^{3/2} + n^{1/2})} = 9.5 \text{ (gc scaling)}$$

for $n = 12$. For a dirty water surface with modules of decay $\frac{1}{4}\sqrt{2}\nu^{1/2}C^{1/2}\kappa^{3/2}$ (versus $2\nu\kappa^2$) (Lamb 1932, section 351), we have

$$\tau = \tau_0 \gamma^{1/2} K' \alpha_c^2$$
$$K'(\kappa) = 2^{-1/2}\kappa_c^{1/2}C_c^{3/2} = 2^{-5/4}(n^{5/6} + n^{-1/6})^{3/4} = 1.86 \text{ (gc scaling)}.$$

Thus,

$$\tau_{clean} = 0.81\ \alpha_c^2, \qquad \tau_{dirty} = 3.9\alpha_c^2 \text{ N/m}^2.$$

These numbers indicate an enormous sensitivity to pollution. For saturation, set $\alpha_c = \alpha_g = 0.3$, which gives

$$\tau = 0.07, \ 0.35 \ \text{N/m}^2.$$

These values represent the stress in regions covered by decaying capillaries. For the average stress we may set $\overline{\tau} = \frac{1}{4}\tau$. These values are much too small for clean water, and dirty water is an unlikely description for open sea conditions.

**7.2.4. Conclusion.** Finite amplitude waves are not symmetrical; slopes on the downwind side of the crest exceed those on the upwind side, which results in a mean cube slope (skewness) that can be detected in the glitter. The classical Stokes solution gives the upward displacement of the crest relative to the mean surface as a function of the first order steepness $\alpha$. To interpret skewness, I have attempted to modify the classical symmetric Stokes wave to allow for corresponding downwind displacement of the crest. The modified Stokes theory then gives $\langle m^2 \rangle$ and $\langle m^3 \rangle$ as functions of $\alpha$, $\beta$, which together with the BH relation $\langle m^3 \rangle = f(\langle m^2 \rangle)$ yield $\beta = f(\alpha)$. $\beta$ remains very small until $\alpha \approx 0.3$, whence it rises sharply to $\beta \approx \alpha \approx 0.3$. This sequence would seem to be reasonable: a forward displacement of the crest by an amount comparable to the crest height, occurring at values of $\alpha$ usually identified with instability. The challenge is to produce dynamic solutions

$$\alpha = \mu(U)t, \quad \beta = \nu(U)t,$$

which on average reproduce the above inferred features, i.e., very small $\nu$ at low $U$, etc. The solutions can be intermittent, like cats paws on the water surface. Intermittency may be the key!

An alternate account of skewness is in terms of the parasitic capillaries on the forward slope of the gravity waves. This account requires a sudden increase in the capillary amplitude (and hence the combined gravity-capillary slope) in step with the development of skewness. However, there is no indication of a corresponding departure from the linear $\langle m^2 \rangle \sim U$ relation.

## 8. SPECULATIONS ON WAVE BREAKING AND WIND DRAG

We conclude that the parasitic capillaries, though important (possibly dominant) contributors to steepness, do not play dominant roles in determining skewness. Further, we conclude that the drag associated with molecular dissipation of the capillaries is negligible. What about wave breaking as candidate for skewness and drag? Sufficient uncertainty and complexity exist to make this candidate an attractive suspect. We refer readers to the important papers by Longuet-Higgins (1982) and Chapron et al. (2001).

In **Figure 22** I plotted for ready comparision the results from numerical, laboratory, and ocean experiments. In numerical experiments with wave groups (Song & Banner 2002), the center wave initially gains energy at the expense of early and late waves. For very small slopes, wave groups are recursive: The wave groups eventually (order 100 wave periods) return to their initial state. Steep wave groups eventually break near the group center. The numerical modeling established a threshold for breaking in terms of a maximum rate of growth per wave period of square slope (order 1%). This threshold sheds light on laboratory experiments by Rapp & Melville (1990), which showed a progression (with initial steepness) from recursion to incipient breaking to spilling to plunging breaking.[10]

---

[10]The terms spilling and plunging were coined as part of a World War II effort on wave prediction for amphibious landings (Sverdrup & Munk 1947). See also Collier's Encyclopedia 1950, p. 398.
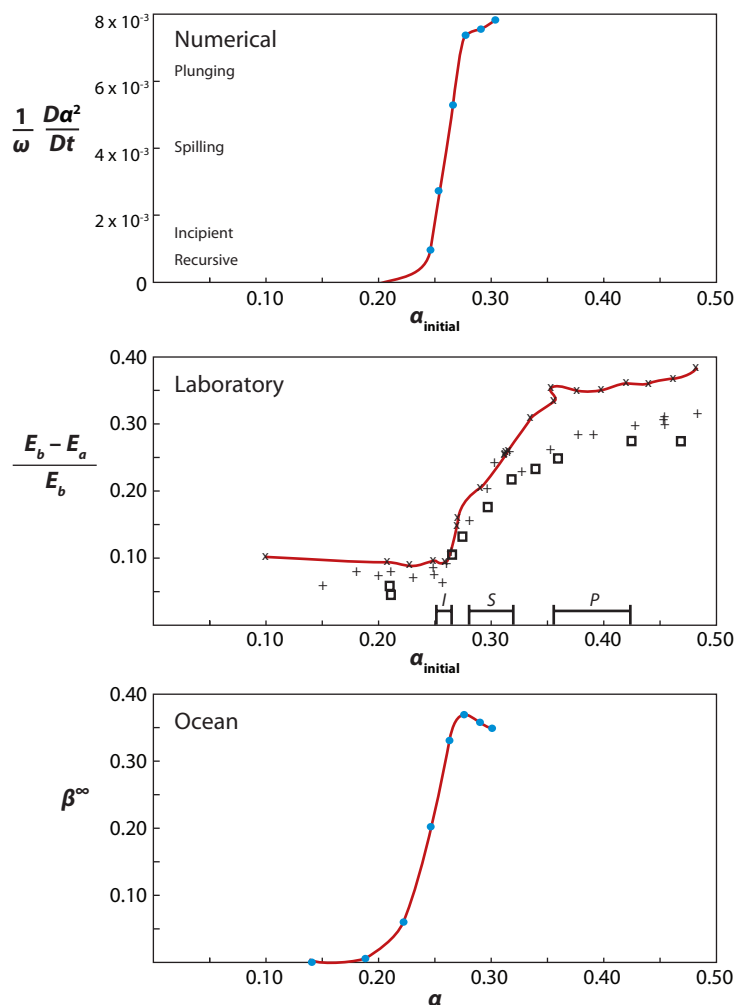
**Figure 22**

(*a*) Numerical experiment that gives maximum growth rate as a function of initial steepness (from Song & Banner 2002, figure 10, with permission). (*b*) Laboratory experiment by Rapp & Melville (1990) that gives fractional energy loss ($E_{a,b}$ is energy after and before breaking event) (from Song & Banner 2002, figure 9). (*c*) Skewness versus root mean square steepness (**Figure 21**).

A comparison of the three data sets is not straightforward. The numerical experiments recorded the rate of growth at the group center of the square slope, and the laboratory experiments recorded the fractional energy dissipated by the breaking waves, both as functions of the initial steepness of the wave group. The BH compilation measures the skewness in terms of the root mean square slope of all waves present. However, the overall resemblance suggests that the rapid onset of skewness with increasing steepness is related to a rapid transition from recursion to incipient to spilling to plunging breakers.

## 8.1. Wind Drag

The wave energy per unit area is

$$E = \frac{1}{2} \rho_w \, g \, a^2. \tag{44}$$

Replace $a^2$ by $\kappa^{-2}(\kappa \, a)^2 = \kappa^{-2} \, \alpha^2$. Rapp & Melville (1990) have measured the fractional energy loss $\phi = \Delta E/E$ by breaking waves as function of initial steepness, $\phi = \phi(\alpha_i)$.

Waves occur in groups of $Q$ waves. Breaking is taken to occur at the modulation maximum, which is at intervals $Q(2\pi/\omega)$. Thus, the mean rate of dissipation is $\dot{E} = \Delta E/(2\pi Q/\omega)$. The associated stress is $\tau = \dot{E}/C$. Putting all this together and allowing for $C^{-1}\omega/\kappa = 1$ and $g \, \kappa^{-1} = C^2$, gives

$$\tau = \frac{1}{4\pi} \, Q^{-1} \rho_w C^2 \alpha^2 \phi. \tag{45}$$

The Hwang measurements (**Figure 11**) suggest $\lambda = 0.2$ m, corresponding to $C = 0.3$ m s$^{-1}$. The Cox-Zhang laboratory measurements (**Table 5**) for $\langle m^2 \rangle = 0.021$ to $0.056$ gave $f = 6.1$ to $3.8$ Hz, or $C = 0.26$ to $0.41$.

A daring step is to set $\phi = \beta$:

$$\tau = \tau_{gc} \frac{1}{4\pi} \, Q^{-1} \, (C/C_{gc})^2 \, \alpha^2 \beta, \quad \tau_{gc} = \rho_w \, C_{gc}^2 = 54.2 \, \text{N/m}^2. \tag{46}$$

I believe $\alpha = \alpha_{brea\,ker}$ is nearly constant. $\tau$ depends almost discontinually on wind speed through $\beta(\alpha)$ and continually through $C(U)$. This suggestion needs much further thought. For an order-of-magnitude estimate we have

$$U = 6 \text{ m/s}, \quad C = 0.3 \text{ m/s}, \quad \langle m^2 \rangle = 0.03, \quad \alpha = 0.24, \quad \beta = 0.06, \quad \tau = 0.0024 \, \text{N/m}^2,$$
$$10 \qquad\qquad 0.4 \qquad\qquad 0.05 \qquad\qquad 0.45 \qquad\quad 0.33 \qquad\quad 0.08$$

as compared with the traditional estimates of 0.05 and 0.09 N/m$^2$ (see **Supplemental Appendix 2**).

## 8.2. Wind Drag Derived from Glitter

The goal is to estimate wind drag from the observed glitter pattern. For example, the image from September 3, 1951 in the Alenuihaha Channel (**Figure 2**, bottom left) is associated with the values

$$\langle m_x^2 \rangle = 0.0230, \quad \langle m_y^2 \rangle = 0.0224, \quad \langle m^2 \rangle = 0.0454, \quad c_{30} = -0.32$$

(Cox & Munk 1956, table 1). The angular downwind displacement of the glitter center is (Equations 7 and 8)

$$(\theta_x)_{\max} = 2(m_x)_{\max} = 2 \sqrt{\langle m_x \rangle^2} \xi_{\max} = 2 \sqrt{\langle m_x^2 \rangle} \frac{1}{2} c_{30} = -0.049$$

or $+2.8°$. For the wind drag we use $Q = 6$, $(C/C_{gc})^2 = 3, \alpha^2 = 2\langle m^2 \rangle = 0.09$ and from **Supplemental Appendix 1** (Moments) $\beta = \frac{2\sqrt{2}}{3} c_{30} = +0.30$, and so $\tau = 0.06$ N/m$^2$. The in situ wind measurement was $U = 8.6$ m s$^{-1}$, yielding $c_D = 0.0014$, $\tau_{total} = 0.10$ N/m$^2$, $\tau_{shear} = 0.05$ N/m$^2$, $\tau_{drag} = \tau_{total} - \tau_{shear} = 0.05$ N/m$^2$ by the traditional method (see **Supplemental Figure 5**). The close agreement is, of course, accidental; there are many, many loose ends. But the intimate connection between skewness and breaking and the suggested $\tau \sim \alpha^2 \beta$ relation offers an alternate route for the remote sensing of wind stress.

## 9. AN INCONVENIENT SEA TRUTH

The incentives for this review are the space-born observations of ocean glitter by Bréon & Henriot (2006). These observations present a few simple, robust rules for the steepness, directional spread, and skewness of surface slopes, confirmed by a very extensive global data set; yet the information is sparse because it says nothing about time and space scales. The BH rules are an inconvenient sea truth, too fundamental to be ignored, too incomplete to be understood.

Slope statistics are governed by waves much shorter than those underlying elevation statistics. I believe that the physical principles underlying the short wave generation are different and distinct from those underlying the generation of the long waves, and not just an extrapolation into high frequencies. From the point of view of ocean dynamics, the short waves are probably more interesting, yet the literature is tiny compared with the extensive literature on the longer, higher surface waves.

With regard to angular spread, the measured two dimensionality can probably be interpreted in terms of some geometric constructs. The spread is wide, and the directional beam pattern appears to have a minimum in the downwind direction. After arguing that the inherent two dimensionality is crucial to any sensible treatment, I promptly move toward a simpler one-dimensional model.

With regard to skewness, circumstantial evidence shows that the near step-like onset is related to a rapid progression from incipient to spilling to plunging breakers as the wind rises above $4 \, \text{m s}^{-1}$.

With regard to steepness, I am troubled by the contrast between the simple BH rule for a linear dependence on wind speed and the complexity of the attempted explanations. The combined contributions of short gravity plus capillary waves, each obeying its own set of laws, does not readily add up to a linear wind dependence and attempted explanations appear contrived. Have we missed some simple underlying phenomenology? Such as the steepness of cats paws generated intermittently at a rate linearly proportional to wind speed? Or the reflection of sunlight from bubbles?

At the 1955 celebration of the 25th birthday of the Woods Hole Oceanographic Institution, I was given the opportunity to review what was then known about our subject (Munk 1955). After referring to the Cox and Munk result of a linear wind dependence of the mean-square slope and its large crosswind component, I spoke of the need for "a respectable theory" of wind drag, and, referring to a recent photograph (reproduced in **Figure 23**), mentioned " . . . how important it is
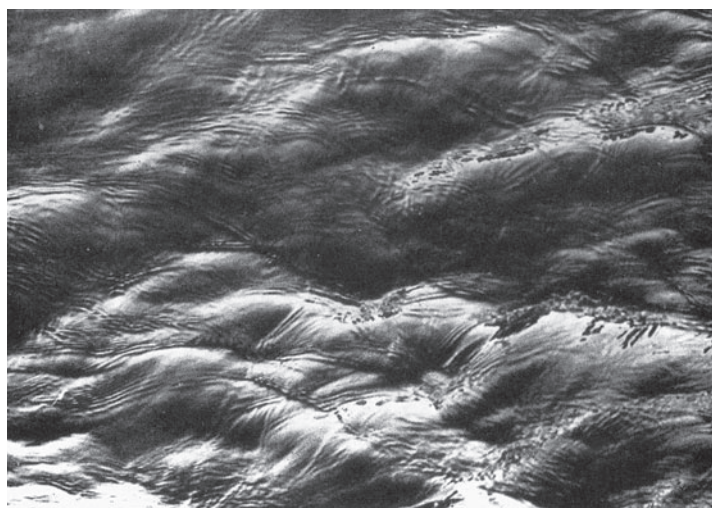


**Figure 23**

This photograph was taken by William van Arx off Woods Hole dock nearly fifty years ago, and was reproduced in Munk (1955). I estimate that the distance across is approximately two meters.

to look at the raw data before deciding on pertinent statistical parameters." How slow progress has been in the past fifty years!

But there is hope. I surmise that the key contributing wave scales range from millimeters to a meter. These are the very scales that will be the subject during the next few years of extensive sea-going experiments, which will use powerful new optical tools. If the time for review is when a subject is under active development, with new solutions being found and old solutions being demolished, not when it is to be tidied and put to rest, then this is indeed the right time for review.

## APPENDIX A: NOTATION

The canonical dispersion relation at the gc transition is in terms of variables relative to their values at minimum phase velocity. Using

$$g = 9.8 \text{ m s}^{-2}, \quad \rho_w = 1025 \text{ kg m}^{-3}, \quad \rho_a = 1.225 \text{ kg m}^{-3}, \quad T = 0.074 \text{ N m}^{-1}$$

we have $T_1 = T/(\rho_w - \rho_a) = 7.23 \times 10^{-5} \text{ m}^3 \text{ s}^{-2}$, and

$$\omega_{gc} = (4g^3/T_1)^{\frac{1}{4}} = 84.9 \text{ rps}, \quad \kappa_{gc} = (g/T_1)^{\frac{1}{2}} = 368 \text{ rpm}$$

$$f_{gc} = \omega_{gc}/2\pi = 13.5 \text{ Hz}, \quad k_{gc} = \kappa_{gc}/2\pi = 58.6 \text{ cpm}, \quad C_{gc} = 0.23 \text{ m/s}.$$

The canonical dispersion law is

$$2C^2 \equiv 2(\omega/\kappa)^2 = \kappa^{-1} + \kappa \qquad \text{gc scaling}$$

with a minimum $C = 1$ at $\omega = 1, \ \kappa = 1$.

## APPENDIX B: POWER SPECTRA

### Elevation

The starting point is the decomposition of mean-square elevation in frequency and wavenumber space:

$$\langle \zeta^2 \rangle = \int_0^\infty F_\zeta(\omega)\, d\omega = \int_{-\infty}^\infty \int_{-\infty}^\infty F_\zeta(\kappa_x, \kappa_y)\, d\kappa_x\, d\kappa_y. \tag{1}$$

In polar wavenumber coordinates $\kappa_x = \kappa \cos\theta, \ \kappa_y = \kappa \sin\theta$,

$$\langle \zeta^2 \rangle = \int_0^\infty \int_{-\pi}^\pi F_\zeta(\kappa, \theta)\kappa\, d\theta\, d\kappa = \int_0^\infty G_\zeta(\kappa)\, d\kappa \tag{2}$$

where

$$G_\zeta(\kappa) = \int_{-\pi}^\pi F_\zeta(\kappa, \theta)\kappa\, d\theta \tag{3}$$

is the one-dimensional (or omnidirectional) spectrum. We factor the directional dependence

$$F_\zeta(\kappa, \theta) = F_\zeta(\kappa)\phi(\theta), \quad \int_{-\pi}^\pi \phi(\theta)\, d\theta = 1. \tag{4}$$

For isotropic radiation, $\phi = 1/(2\pi)$. From Equations 1 and 2,

$$G_\zeta(\kappa) = \kappa \ F_\zeta(\kappa) = F_\zeta(\omega) \cdot d\omega/d\kappa, \quad \omega = \omega(\kappa)$$

$$= \frac{1}{2}g\omega^{-1}F_\zeta(\omega), \quad \omega^2 = g\kappa \text{ gravity waves.} \tag{5}$$

We take a low-frequency cut-off (waves do not outrun the wind) for $C = \mu\, U$, or

$$\langle \zeta^2 \rangle = \int_{\omega_0}^{\infty} F_\zeta(\omega)\, d\omega = \int_{\kappa_0}^{\infty} G_\zeta(\kappa)\, d\kappa, \quad \omega_0 = g/\mu U, \quad \kappa_0 = g/(\mu U)^2.$$

To transfer from the circular frequencies $\omega,\ \kappa$ to the cyclical frequencies $f, k$, we have

$$\langle \zeta^2 \rangle = \int_0^{\infty} F(\omega)\, d\omega = \int_0^{\infty} F(f)\, df = \int_0^{\infty} G(\kappa)\, d\kappa = \int_0^{\infty} G(k)\, dk$$

and so

$$F[f] = 2\pi\, F[\omega(f)],\, G[k] = 2\pi\, G[\kappa(k)], \quad \omega(f) = 2\pi f, \quad \kappa(k) = 2\pi k. \tag{6}$$

## Slope

The slope spectrum has the components

$$F_{m_x}(\kappa) = (\kappa \cos\theta)^2\, F_\zeta(\kappa), \quad F_{m_y}(\kappa) = (\kappa \sin\theta)^2\, F_\zeta(\kappa)$$

so that $F_m(\kappa) = \kappa^2\, F_\zeta(\kappa)$, $\langle m^2 \rangle = \langle m_x^2 \rangle + \langle m_y^2 \rangle$, and similarly for $G(\kappa)$.

## DISCLOSURE STATEMENT

The author is not aware of any biases that might be perceived as affecting the objectivity of this review.

## ACKNOWLEDGMENTS

## LITERATURE CITED

Banner ML, Jones ISF, Trinder JC. 1989. Wavenumber spectra of short gravity waves. *J. Fluid Mech.* 108:321–44

Banner ML. 1990. Equilibrium spectra of wind waves. *J. Phys. Ocean.* 20:966–84

Banner ML, Chen W, Walsh EJ, Jensen JB, Lee S, Fandry C. 1999. The Southern Ocean Wave Experiment. Part I: Overview and mean results. *J. Phys. Ocean.* 29:2130–45

Bréon FM, Henriot N. 2006. Spaceborne observations of ocean glint reflectance and modeling of wave slope distributions. *J. Geophys. Res.* 111:C06005

Chapron B, Kerbaol V, Vandemark D, Elfouhaily T. 2000. Importance of peakedness in sea surface slope measurements and application. *J. Geophys. Res.* 105:17195–202

Chapron B, Vandemark D, Elfouhaily T. 2002. On the skewness of the sea slope probability distribution. *AGU Monogr.* Vol. 127. pp. 59–63, ed. MA Donelan, WM Drennan, ES Satzman, R Wanninkhof. Washington, DC: AGU Press.

Cox C. 1958. Comments on Dr. Phillip's Paper. *J. Mar. Res.* 16(3):241–45

Cox C, Munk W. 1956. Slopes of the sea surface deduced from photographs of sun glitter. *Scripps Inst. Oceanogr. Bull.* 6(9):401–88

Donelan MA, Hamilton J, Hui WH. 1985. Directional spectra of wind-generated waves. *Philos. Trans. R. Soc. London Ser. A* 315:509–62

Ekman VW. 1905. On the influence of the Earth's rotation on ocean currents. *Arkiv. Mat. Astr. Phys.* 2:53

Elfouhaily T, Chapron B, Katsaros K, Vandemark D. 1997. A unified directional spectrum for long and short wind-driven waves. *J. Geophys. Res.* 102(C7):15781–96

Haubrich RA, Munk WH, Snodgrass FE. 1963. Comparative spectra of microseisms and swell. *Bull. Seism. Soc. Am.* 53(1):27–37

Hughes B. 1976. Estimates of underwater sound (and infrasound) produced by nonlinearly interacting ocean waves. *J. Acoust. Soc. Am.* 60:1032–39

Hwang PA. 2005. Wave number spectrum and mean square slope of intermediate-scale ocean surface waves. *J. Geophys. Res.* 110:C10029

Jahne B, Riemer. 1990. Two-dimensional wavenumber spectra of small-scale water surface waves. *J. Geophys. Res.* 95:11531–46

Keulegan GH. 1951. Wind tides in small closed channels. *J. Res. Nat. Bur. Stand.* 46:351–81

Lamb H. 1932. *Hydrodynamics*. Cambridge, UK: Cambridge Univ. Press. 6th ed.

Longuet-Higgins MS. 1950. A theory of microseisms. *Phil. Trans. R. Soc.* 243:1–35

Longuet-Higgins MS. 1995. Parasitic capillary waves: a direct calculation. *J. Fluid Mech.* 301:79–107

Longuet-Higgins MS. 1982. On the skewness of sea-surface slopes. *J. Phys. Oceanogr.* 12:1283–91

McCreery CS, Duennebier FK, Sutton GH. 1993. Correlation of deep ocean noise (0.4–30 Hz) with wind, and the Holu specrum—a worldwide constant. *J. Acoust. Soc. Am.* 93:2639–48

Miles JW. 1957. On the generation of surface waves by shear flows. *J. Fluid Mech.* 3:185–204

Munk W. 1955. High-frequency spectrum of ocean waves. *WHOI Convocation, J. Mar. Res.* 14(4):302–14

Neumann G. 1953. On ocean waves spectra and a new method of forecasting wind-generated sea. *Beach Erosion Board Tech. Mere.* No. 43. 42 pp.

Phillips OM. 1957. On the generation of waves by turbulent wind. *J. Fluid Mech.* 2:417–45

Phillips OM. 1958. The equilibrium range in the spectrum of wind-generated waves. *J. Fluid Mech.* 4:426–34

Phillips OM. 1985. Spectral and statistical properties of the equilibrium range in wind-generated gravity waves. *J. Fluid Mech.* 156:505–531

Rapp RJ, Melville WK. 1990. Laboratory measurements of deep water breaking waves. *Phil. Trans. R. Soc. London Ser. A* 331:735–800

Song J, Banner ML. 2002. On determining the onset and strength of breaking for deep water waves. Part 1: unforced irrotational wave groups. *J. Phys. Oceanogr.* 32:2541–58

Spooner J. 1822. Sur la lumière des ondes de la mer. *Corresp. Astro. Baron Zach.* 6:331

Sverdrup H, Munk W. 1947. *Wind, Sea, and Swell: Theory of Relations for Forecasting. Tech. Rep. 1, Publ.* 601. Washington, DC: U.S. Hydrogr. Off. 44 pp. (Classified publication September 1943).

Thompson W. (Lord Kelvin) 1887. On ship waves. *Proc. Inst. Mech. Eng.* pp. 409–433; also 1891. *Popul. Lect. Addresses*, II:450–500

Tyler GL, Teague CC, Stewart RH, Peterson AM, Munk WH, Joy JW. 1974. Wave directional spectra from synthetic aperture observations of radio scatter. *Deep-Sea Res.* 21:989–1016

Van Dorn WG. 1953. Wind stress on an artificial pond. *J. Mar. Res.* 12:249–76

Veron F, Melville WK. 2001. Experiments on the stability and transition of wind-driven water surfaces. *J. Fluid Mech.* 446:25–65

Webb S, Cox CS. 1986. Observations and modeling of seafloor microseism. *J. Geophys. Res.* 91(B7):7343–58

Wentz FJ. 1976. Cox and Munk's sea surface slope variance. *J. Geophys. Res.* 81:1607–8

Yuen HC, Lake BM. 1980. Instabiltities of waves in deep water. *Annu. Rev. Fluid Mech.* 2:303–334

Zakharov VE, Rubenchik AM. 1973. Instability of waveguides and solitons in nonlinear media. *Zh. Eksp. Teor. Fiz.* 65:997–1011; 1974. Transl. *Sov. Phys. JETP* 38:494–500